



Delft University of Technology

Infrasound reveals detailed eruptive processes at Nyiragongo volcano and enhances monitoring capabilities during unrest periods

Barrière, Julien; Oth, Adrien; Assink, Jelle; d'Oreye, Nicolas; Evers, Läslö

DOI

[10.1038/s43247-025-02937-3](https://doi.org/10.1038/s43247-025-02937-3)

Publication date

2025

Document Version

Final published version

Published in

Communications Earth and Environment

Citation (APA)

Barrière, J., Oth, A., Assink, J., d'Oreye, N., & Evers, L. (2025). Infrasound reveals detailed eruptive processes at Nyiragongo volcano and enhances monitoring capabilities during unrest periods. *Communications Earth and Environment*, 6(1), Article 978. <https://doi.org/10.1038/s43247-025-02937-3>

Important note

To cite this publication, please use the final published version (if applicable).

Please check the document version above.

Copyright

Other than for strictly personal use, it is not permitted to download, forward or distribute the text or part of it, without the consent of the author(s) and/or copyright holder(s), unless the work is under an open content license such as Creative Commons.

Takedown policy

Please contact us and provide details if you believe this document breaches copyrights.

We will remove access to the work immediately and investigate your claim.



Infrasound reveals detailed eruptive processes at Nyiragongo volcano and enhances monitoring capabilities during unrest periods



Julien Barrière ¹✉, Adrien Oth ¹, Jelle Assink ², Nicolas d'Oreye ^{1,3} & Láslo Evers ^{2,4}

Eruptions at continental basaltic volcanoes can take and combine various forms, including lava lakes, lava flows and fountaining, explosions or structural collapses. Aside from a few well-instrumented cases worldwide, accurately reconstructing eruptive scenarios is hampered by the lack of detailed visual observations. However, volcanoes also have their own acoustic signatures composed of low-pitched inaudible sounds, called infrasounds. Here we analyze infrasound records close to Nyiragongo volcano (D.R. Congo) (<20 km) up to Kenya (~800 km), which are converted using acoustic numerical modeling into time-lapse observations of the catastrophic drainage of the world's largest lava lake on 22 May 2021. The emitted infrasounds also enable tracking of fissure openings and lava eruptions along the flank, occurring simultaneously with the lava lake drainage. This striking example supports the growing role of infrasound as a key component of volcano monitoring and early-warning systems, as it provides unique information inaccessible to other ground-based instruments.

Active basaltic volcanism, which is the dominant mode of volcanism on Earth, is characterized by low-viscosity lavas and frequent to persistent eruptions¹. It includes some of the most famous and well-instrumented volcanoes and regions on Earth, e.g., Iceland, Kilauea (Hawaii), Etna, or Stromboli (Italy). Recording seismicity is widely recognized as essential for tracking magma movements at depth^{2,3} but must be complemented with other observations for monitoring eruptions, which are by essence atmospheric processes. Short-range and high frame rate visible/infrared camera recordings can provide essential insights into the eruptive processes and their timing^{4–7}. In the absence of such visual monitoring tools or if the view is hampered by clouds (including volcanic ashes from the eruption itself), infrasound (acoustic waves <20 Hz) may be the only way to capture timely information on new or changing eruptive stages. At local distance, generally defined within 15 km from the active vent(s)^{8,9}, numerous studies over the past two decades have investigated the acoustic signature of volcanic eruptions over long periods of time (months to years), with strong implications for monitoring aspects, e.g., at Kilauea (Hawaii)^{10,11}, Etna (Italy)^{12,13}, Stromboli (Italy)^{14,15}, Villarica (Chile)¹⁶ or Nyiragongo (D.R. Congo)^{17,18}. Moreover, infrasound may propagate over long distance in the atmosphere, thus

offering the opportunity of monitoring eruptive activity from regional (15–250 km) to global distance^{8,19}. Violent explosive eruptions (i.e., Vulcanian–Plinian), which are not characteristic of the aforementioned basaltic volcanoes, are the more prone to generate long-range signals¹⁹. This includes remote volcanoes such as Hunga Tonga–Hunga Ha'apai (Tonga)²⁰, Eyjafjallajökull (Iceland)²¹, or Yasur (Vanuatu)²². Nevertheless, powerful Strombolian explosions were also successfully monitored over hundreds of km from typical basaltic volcanoes, e.g., at Stromboli²³ or Etna²⁴. On another hand, Hawaiian-like eruptions (e.g., lava lake, lava fountaining) require local observations, such as encountered at Kilauea^{10,11,25} or Nyiragongo^{17,18,26} for characterizing low-level infrasonic tremors due to persistent intra-crater effusive eruptive activity.

We focus in this study on the last-mentioned volcano located in the Kivu rift (East Africa), which is a remarkable extensional continental setting characterized by active tectonic and magmatic processes. Nyiragongo is one of the most active volcanoes on Earth²⁷. Effusive activity within its ~1.2 km wide crater takes most of the time the form of a long-lived lava lake, of which the dimensions reached 200 m in diameter and 300 m deep in early 2021, making this lava lake the largest on Earth at that time²⁸. In the past two decades, days-long experiments within its crater (degassing^{29,30}, thermal^{26,31},

¹European Center for Geodynamics and Seismology, Walferdange, Luxembourg. ²Royal Netherlands Meteorological Institute, De Bilt, The Netherlands. ³National Museum of Natural History, Walferdange, Luxembourg. ⁴Delft University of Technology, Delft, The Netherlands. ✉e-mail: julien.barriere@ecgs.lu

infrasound²⁶, seismic³²) and long-term monitoring deployments around the edifice (seismic^{18,28,33}, infrasound^{17,18}, degassing³⁴) have led to an increasing understanding of the lava-lake convective processes maintaining large volume of molten lava within its pit crater. Such ground-based observations were also sometimes coupled with space-based measurements (Synthetic-Aperture-Radar^{17,18,28,35}, thermal imagery^{17,31}, SO₂ degassing^{17,32,33,35}), which allow extending the observational window both in time and space, though their temporal sampling rate (daily at best) is much lower than the ones from ground measurements (milliseconds to minutes). Also, seismic^{28,32,36,37} and petrological^{38,39} investigations all converge to a plumbing architecture formed by a deep reservoir (9–15 km depth) well connected to the lava-lake system, as evidenced by the piezometer-like behavior of the lava-lake level reacting synchronously with pressure variations induced by deep (>10 km b.s.l.) magmatic intrusions^{28,32,40}.

On 22 May 2021, the drainage of Nyiragongo's lava lake was accompanied by lava flows from eruptive fissures toward a one-million urban area composed of the cities of Goma (D.R. Congo) and Gisenyi (Rwanda)³⁵ (Fig. 1 and Supplementary Fig. S1). After 1977 and 2002, this was the third known flank eruption and the first one adequately monitored with seismic

and geodetic instruments to understand magma movements at depth. A probable scenario supported by these geophysical observations is the rupture of the edifice, starting around 15:57 UTC (all times are given as UTC time from here), draining the lava lake and initiating a week-long magmatic intrusion (dyke) in the Earth's crust³⁵ (Fig. 1a). Visual accounts of lava outburst on the flank were reported tens of minutes later, which shocked the nearby population⁴¹ due to the absence of clear precursory seismicity or ground deformation hours, days or weeks before^{35,42}. The subsequent migration of magma at shallow depth, accompanied by moderate-size earthquakes directly beneath the city of Goma strongly contributed to a dramatic humanitarian crisis with hundreds of casualties and chaotic population movements^{35,41} (Fig. 1). In this study, we use infrasound sensors for inferring the main eruptive processes during the very first hours of the eruption on 22 May 2021. Three stations (NYI, KBTI, GOM) deployed at local to near-regional distances (approx. 0.6, 6, and 18 km from Nyiragongo's main crater/lava-lake) are co-located with broadband seismometers (Fig. 1). Moreover, we investigate long-range records more than 800 km away at the infrasound array I32KE in Nairobi (Kenya), which is part of the International Monitoring System (IMS)^{8,43} (see “Methods”).

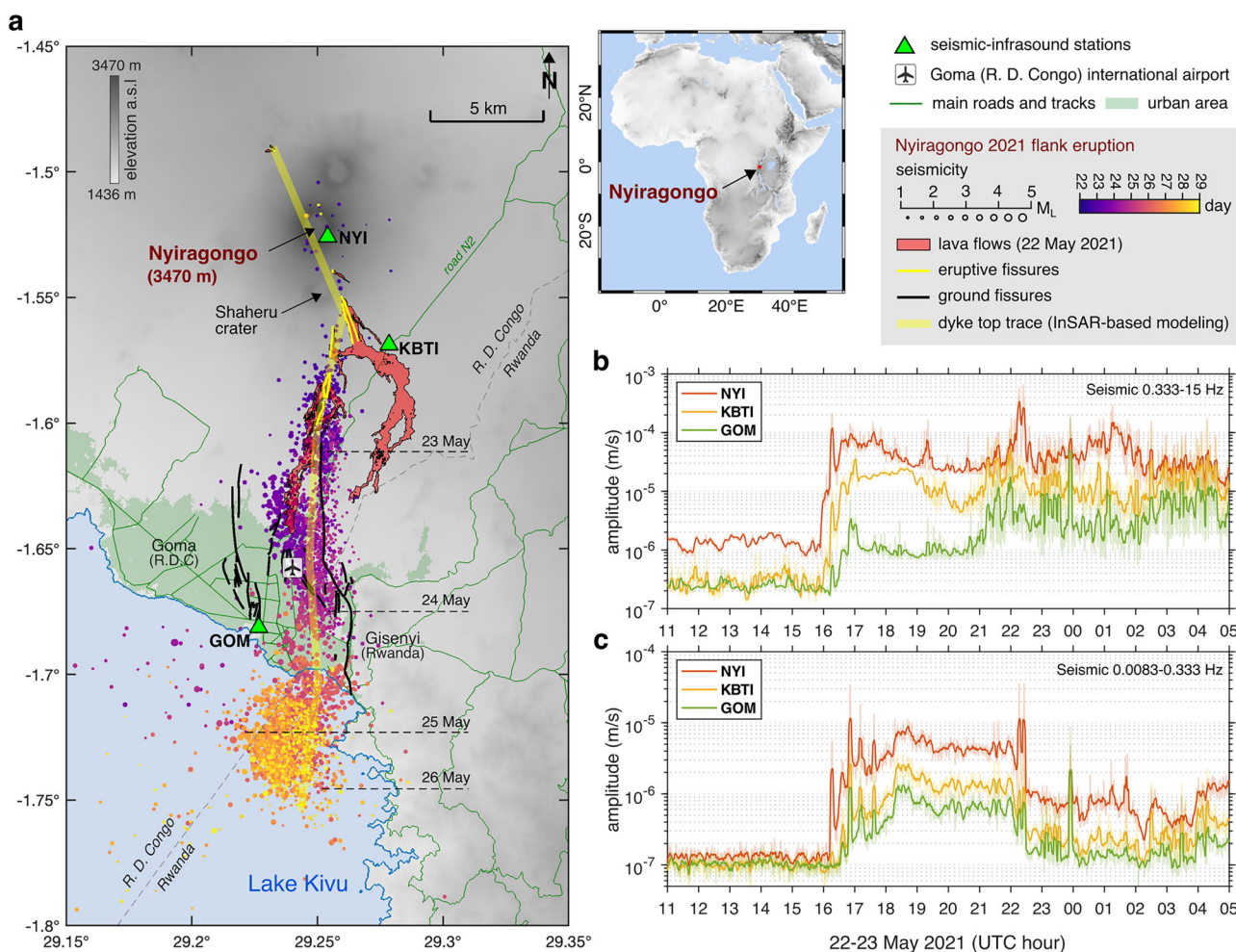


Fig. 1 | The May 2021 Nyiragongo flank eruption. **a**, Map of Africa situating Mount Nyiragongo and zoom into the study area. Local stations (KivuSNet network³⁰) with co-located seismic and infrasound sensors are depicted as green triangles. Data for the Nyiragongo 2021 flank eruption³⁵ are the seismic events over time (blue to yellow from 22 to 28 May 2021, with marker size corresponding to the magnitude between 1 and 5, minimum latitudes along the path of the dyke at 00:00 UTC on 23, 24, 25 and 26 May are indicated by horizontal black dashed lines); the lava flows (red area); the eruptive fissures (yellow lines); the ground fissures detected from Interferometric Synthetic Aperture Radar (InSAR) (black lines); the dyke top trace connected to eruptive fractures (thick

transparent yellow line) obtained from InSAR modeling. The main roads (green lines) are plotted from datasets available at the WFPgeonode (<https://geonode.wfp.org>). The boundary R. D. Congo/Rwanda (dashed gray line) is plotted according to the 2015 GADM database (<https://gadm.org>). The background topography (shaded gray) is derived from SRTM data with 1 arc-s resolution (NASA/USGS). RMS seismic amplitude time series between 11:00 on 22 May and 05:00 on 23 May for frequency bands **(b)** 0.333–15 Hz and **(c)** 0.0083–0.333 Hz at stations NYI, KBTI, and GOM. 1-min RMS amplitude time series are plotted in background and moving averages over centered 5-min windows are plotted as thick lines. Note that the y-scale is logarithmic.

Results and discussion

How infrasound relates to seismicity during the eruption

Infrasound and seismic records, either associated to single events (e.g., explosion, earthquakes), tremor (i.e., continuous excitation or overlapping events), or both, provide highly complementary information about volcanic processes. Volcanoes hosting active lava lakes are so-called open-vent because depressurization of the magmatic system is possible through continuous degassing, which generates coupled infrasound and seismic signals from near-surface processes^{44,45}. Over decades at Nyiragongo, persistent lava lake activity (i.e., spattering, bubble bursting, convective flow) had generated sustained broadband seismic tremor^{32,33,46}, which is also detectable in infrasound records^{17,18}, in the frequency band 0.333–15 Hz (i.e., wave periods below 3 s). Such non-destructive repetitive process at shallow depth is characteristic of lava-lake volcanoes such as Kilauea (Hawaii)^{47,48}, Ert A Ale (Ethiopia)^{49,50}, or Villarica (Chile)^{51,52}. In the same frequency band at Nyiragongo, swarms of earthquakes are detected during several episodic deep (>10 km b.s.l.) magmatic intrusions^{28,32,40} and at shallowest level during the last May 2021 flank eruption³⁵. On a general level at active volcanoes worldwide, in the band 0.333–15 Hz, signals with dominant low-frequency content are interpreted as due to fluid-driven source mechanisms in contrast with higher-frequency signals generated by brittle-failure mechanisms^{2,3}. However, the discrimination of seismic source mechanisms at volcanoes based solely on the signal's frequency content is not straightforward^{2,3,53,54}, as observed at Nyiragongo where deep repetitive events of magmatic origin can share the same high-frequency signature as typical volcano-tectonic earthquakes³². Low-frequency signal could also reflect seismic path effects between the hypocenter and the station without the need of fluid involved in the source mechanisms^{53,54}. For now, a comprehensive classification of seismic signals assigning source mechanisms at Nyiragongo is unavailable⁴². However, based on some of the above-mentioned studies at Nyiragongo^{18,28,32,33,35,46}, we can assume that the continuous seismic amplitude filtered in the band 0.333–15 Hz is representative of magmatic and (volcano-)tectonic processes in the area (Fig. 1b), and local noise sources of human origin at KBTI and GOM (Supplementary Fig. S2)⁴².

On 21 May 2021, before 15:57, the band 0.333–15 Hz contained the well-known seismo-acoustic tremor caused by the persistent lava-lake activity at Nyiragongo (Supplementary Figs. S2–3). After 15:57, increase of 0.333–15 Hz seismicity is first detected at the edifice (Fig. 1b and Supplementary Fig. S2), then detected across the local seismic network after 16:15³⁵. The spatial distribution of seismic events detected within the same frequency range (Fig. 1a) reveals a major dyke intrusion through the Earth's crust, as the magma progressed from the crater toward Lake Kivu³⁵. At midnight on 23 May, the tip of the dyke, as inferred by seismic epicenters, already progressed ~10 km further to the south with respect to Nyiragongo's crater (Fig. 1a). This major magmatic intrusion can also be inferred by the sustained increase in continuous amplitude measurements at stations farther from the summit⁴², particularly clear during the first hours of the eruption in the comparative evolution of NYI and GOM amplitude time series (Fig. 1b).

At frequency lower than 0.333 Hz (i.e., wave periods above 3 s), so-called very-long period (VLP) seismicity is frequently observed at active volcanoes^{36,55–62} and is generally attributed to gas/fluid movements at shallow depth beneath the volcano. At Nyiragongo, a marked increase in VLP amplitude within the 3–120 s period range (0.0083–0.333 Hz) is observed coinciding with the onset of the eruption (Fig. 1c). In contrast to the 0.333–15 Hz band, seismicity in the VLP band began to decrease around 22:30 witnessed at all stations, suggesting a potential change within Nyiragongo's edifice rather than along the dyke's propagation path. The generation of VLP signals can be attributed to different source mechanisms operating across a broad frequency range, e.g., as modeled for caldera collapse^{57,58,60} or gas slug ascent^{55,59,61}, either associated with infrasound signals or not. At lava lake volcanoes, the resonance of waves within the magmatic plumbing system—triggered by perturbations at the lava-lake level such as rockfalls, gas bursts, or convection—has been modeled at both Kilauea^{63,64} and Nyiragongo³⁶. At Nyiragongo, several shallow VLP events

were localized at Nyiragongo's crater in 2019–2020, presumably induced by the sloshing of lava in the lake due to degassing bursts or rockfalls³⁶. In particular, a 76 s VLP mode was modeled as the coupling between the lava-lake bottom and a deep reservoir (8–16 km depth) through a magma-filled conduit³⁶.

In Fig. 2, we investigate in more detail how infrasound correlates with seismicity at the summit station NYI. According to the spectrogram analysis of the 2021 eruption and the 2019–2020 seismic observations of VLPs³⁶ (Supplementary Figs. S2 and S4), the VLP band can be further divided into two sub-bands 0.0083–0.025 Hz (i.e., periods of 40–120 s) and 0.025–0.33 Hz (i.e., 3–40 s). Also based on the corresponding spectrograms (Supplementary Fig. S3), infrasound signals are analyzed within two frequency bands, 0.1–1 Hz and 1–10 Hz. The first increase of seismic amplitude at 15:57 in the 0.333–15 Hz band is accompanied by a noticeable increase in 40–120 s VLP band without associated infrasound. 16:15 marks the first notable seismic amplitude peak impacting the whole frequency band. After 16:30, all bandpass-filtered seismo-acoustic signals clearly exhibit higher amplitude than the previous 1-year 10–90th percentile range. Right before 22:30, a double peak is noticeable in every record. After 22:30, both the VLP and infrasound amplitudes drop but remain above the pre-eruptive background levels. Between 16:30 and 22:30, the synchronicity between the increases and peaks of 3–40 s VLP and 0.1–1 Hz infrasound amplitudes is particularly striking. Looking in detail at the largest seismo-acoustic peak around 16:50 (Supplementary Fig. S5), an infrasound signal was detected at the onset of the VLP at station NYI. The detection time at KBTI ~6 km away on the flank is in accordance with a source at the main crater propagating at the speed of sound in the atmosphere (~340 m/s). The 76 s mode observed for the 2019–2020 VLPs³⁶ is also detected. Using infrasound data available in 2019–2020, our analysis confirms that 2019–2020 VLPs were also associated with acoustic onsets (Supplementary Fig. S4) as observed during the eruption (Supplementary Fig. S5), hence supporting the hypothesis of a shallow trigger at the lava-lake level generating VLP signals at Nyiragongo.

From spaceborne synthetic-aperture radar (SAR) images acquired on 22 May at 15:37, we know that the pit crater was still filled with lava 20 min before the start of the seismic unrest⁶⁵. Another SAR observation acquired on 23 May at 04:03 shows an empty crater enlarged by about 1.5 times its previous size (Fig. 2 and Supplementary Fig. S6). During this eruptive period marked by important changes at the summit crater and within the plumbing system, the triggering and source mechanisms of VLP and infrasound signals are likely multifaceted (e.g., rockfalls or bubble explosion at the lava lake surface, gas slug bursting in the shallow conduit, pit-crater floor and walls collapse). Contrary to the complex time-varying spectral content of seismic records (Supplementary Fig. S2), infrasound signals during the 2021 Nyiragongo flank eruption exhibit a clear, yet atypical, dominant frequency content gliding between 1 and 0.1 Hz between 16:30 and 22:30 (Supplementary Fig. S3). Understanding this infrasound signature is the key to unravel the surface eruptive processes between these two epochs.

Modeling the infrasonic harmonic tremor originating from the crater

The frequency gliding pattern was equally observed both in local records and over 840 km away at station I32KE in Kenya (Supplementary Figs. S8 and S9). We retrieve coherent signals between station pairs using cross-correlation, which are characterized by time lags indicating a source at Nyiragongo's crater and two distinct frequency peaks gliding simultaneously (Fig. 3 and "Methods"). These observations suggest the generation of infrasonic harmonic tremor at the summit, as observed at other open-vent volcanoes worldwide, e.g., Kilauea (Hawaii)^{10,25} or Villarica (Chile)¹⁶. Under persistent excitation of its lava lake generating infrasound, Nyiragongo can act as a gigantic acoustic resonator, as already established during decameter lava-lake drops in 2016–2018¹⁸. For instance, deepening the lava-lake would lower the tone of the pit crater as its resonant frequency decreases^{16,18}. Only one resonant mode with sufficient amplitude, assimilated to the fundamental one, can generally be observed at local distance at

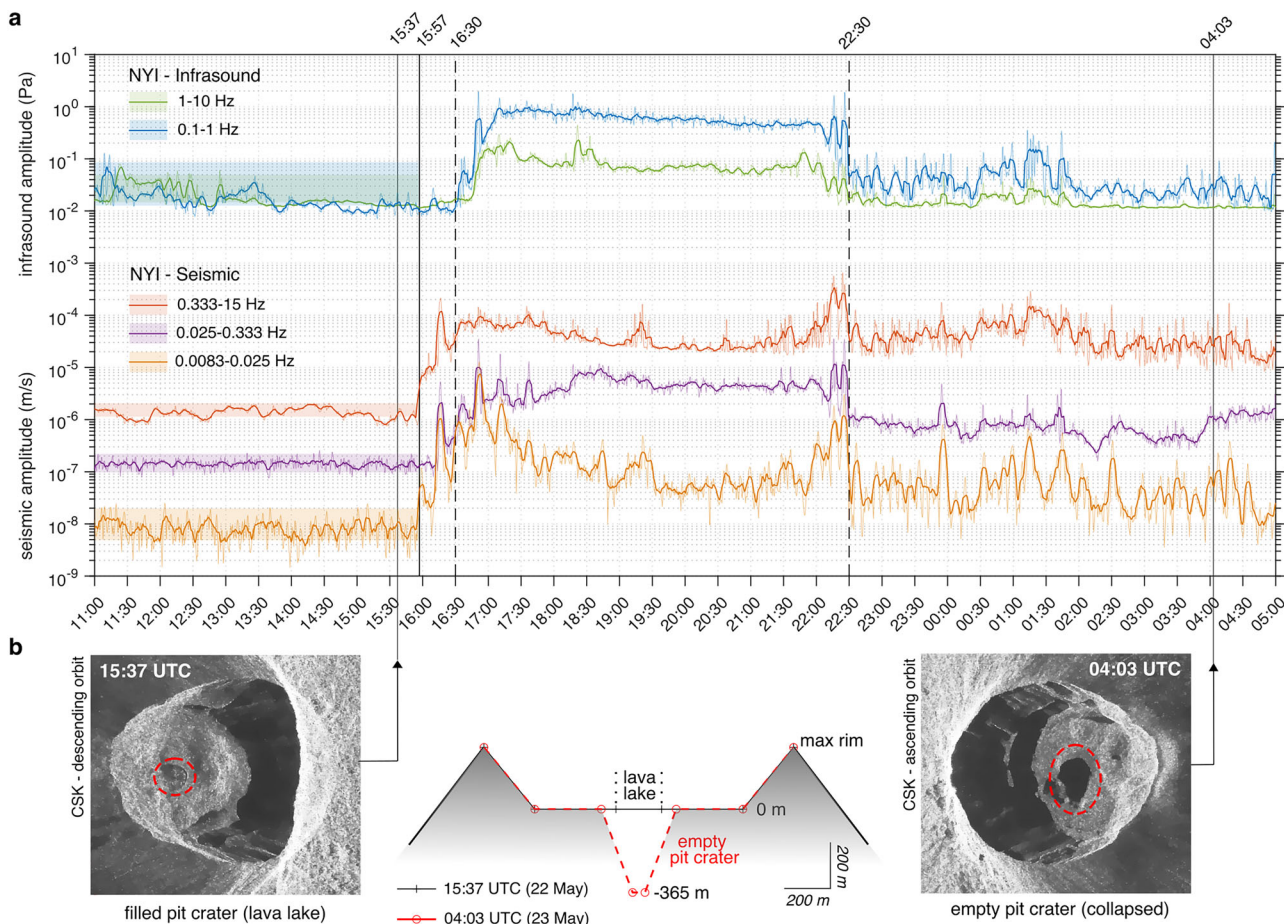


Fig. 2 | Infrasound vs. seismicity in the first hours of the eruption. **a** RMS amplitude time series at NYI filtered in frequency bands 0.1–1 and 1–10 Hz for infrasound, 0.0083–0.025 Hz (40–120 s), 0.025–0.333 Hz (3–40 s) and 0.333–15 Hz for seismic records. 1-min RMS amplitude time series are plotted in background and moving averages over centered 5-min windows are plotted as thick lines. Note that the *y*-scale is logarithmic. The vertical solid line marks the start of abnormal seismicity detected at the summit (15:57), the two vertical dashed lines mark the plateau of infrasound amplitude between 16:30 and 22:30. The constant interval plotted in

transparency for each time series between 11:00 and 15:57 corresponds to the 1-year 10–90th percentile range of 1-min RMS amplitude at NYI between 22 May 2020 and 22 May 2021. **b** Two SAR amplitude images (COSMO-SkyMed) in radar geometry are displayed at acquisition time 15:37 on 22 May (descending orbit) and 04:03 on 23 May (ascending orbit). The sketch in between is a very simplified cross-section view of Nyiragongo's edifice depicting the intra-crater changes between both satellite images. SAR images are processed with the AMSTER software¹⁰⁴.

open-vent volcanoes^{16,66–69}, making this long-range observation of two resonant frequencies remarkable and further referred to as the fundamental frequency (f_0) and the first overtone (f_1).

Following the musical analogy, an interesting outcome is to describe volcanic craters with resonator models such as a closed organ pipe^{16,68} or a Bessel horn⁵¹ for estimating the time-varying depth of the crater (defined as the bottom crater or the lava-lake level if filled). Outperforming such simple (analytical) models, Watson and co-authors^{66,67,69} developed an efficient numerical scheme, called *CRes*⁷⁰, for simulating quasi-1D wave propagation along depth inside an axisymmetric volcanic crater. Nyiragongo's crater as defined in our simulation is the pit crater containing the lava lake. The pit crater, which is about 300-m deep and 200-m wide, can be reasonably considered as axisymmetric despite being slightly elliptical²⁸. The dimensions of the pit crater are of the same order of magnitude as the dimensions of the main crater at other open-vent volcanoes (e.g., Etna⁴⁶, Villarica¹⁶, Erebus⁷¹). At Nyiragongo, the main crater (hosting the pit crater) is much larger (about 1.2 km wide) and is only 200–250 m deep (difference of altitude between the rim of the pit crater and the rim of the main crater). The contrast of impedance (i.e., the ratio of acoustic pressure to acoustic flow) at the crater outlet describes the resistance to flow. It determines if acoustic waves are preferentially reflected inside the crater or are radiated outside. For acoustic resonance to occur, the impedance contrast must be high, which occurs when the crater radius is small compared to the infrasound

wavelength and the crater depth is comparable to the wavelength⁶⁷. For realistic sources with energy at frequencies below 1 Hz^{16,66}, the conditions to excite resonant modes in Nyiragongo are met for its pit crater, but not for its main crater (Supplementary Fig. S11). Hence, the acoustic radiation from the crater outlet to any receiver starts in our simulation at the top of the pit crater and reflection inside the main wide crater is not considered (see “Methods”).

We set up an inversion strategy for both f_0 and f_1 using *CRes* to determine the pit-crater geometry (see “Methods”). The variations of f_0 and f_1 with time follow monotonically decreasing functions (Fig. 4). Simultaneously inverting these two interrelated resonant frequencies strongly constrains the evolving crater geometry defined by its width and depth, which either increase or stabilize with time during the drainage of the lava lake (see “Methods”). SAR observations between January 2002 and May 2021 allow to define an initial pit crater model with an estimated depth of about 300 m at the time of the eruption²⁸ (Fig. 4 and “Methods”). According to SAR observations on 22–23 May 2021⁶⁵ (Fig. 2), we allow the radii of the simplified pit-crater geometry to widen uniformly by a factor ranging from 1 to 1.5 (i.e., upper radius from 110 to 165 m) and let the depth free to get any values down to 500 m. For each successive time step, we look for the best-fit model explaining both f_0 and f_1 . The final time-dependent models depicted in Fig. 4 converge to similar solutions. The resulting, most likely scenario is a fast complete draining of lava from the crater in less than one hour between

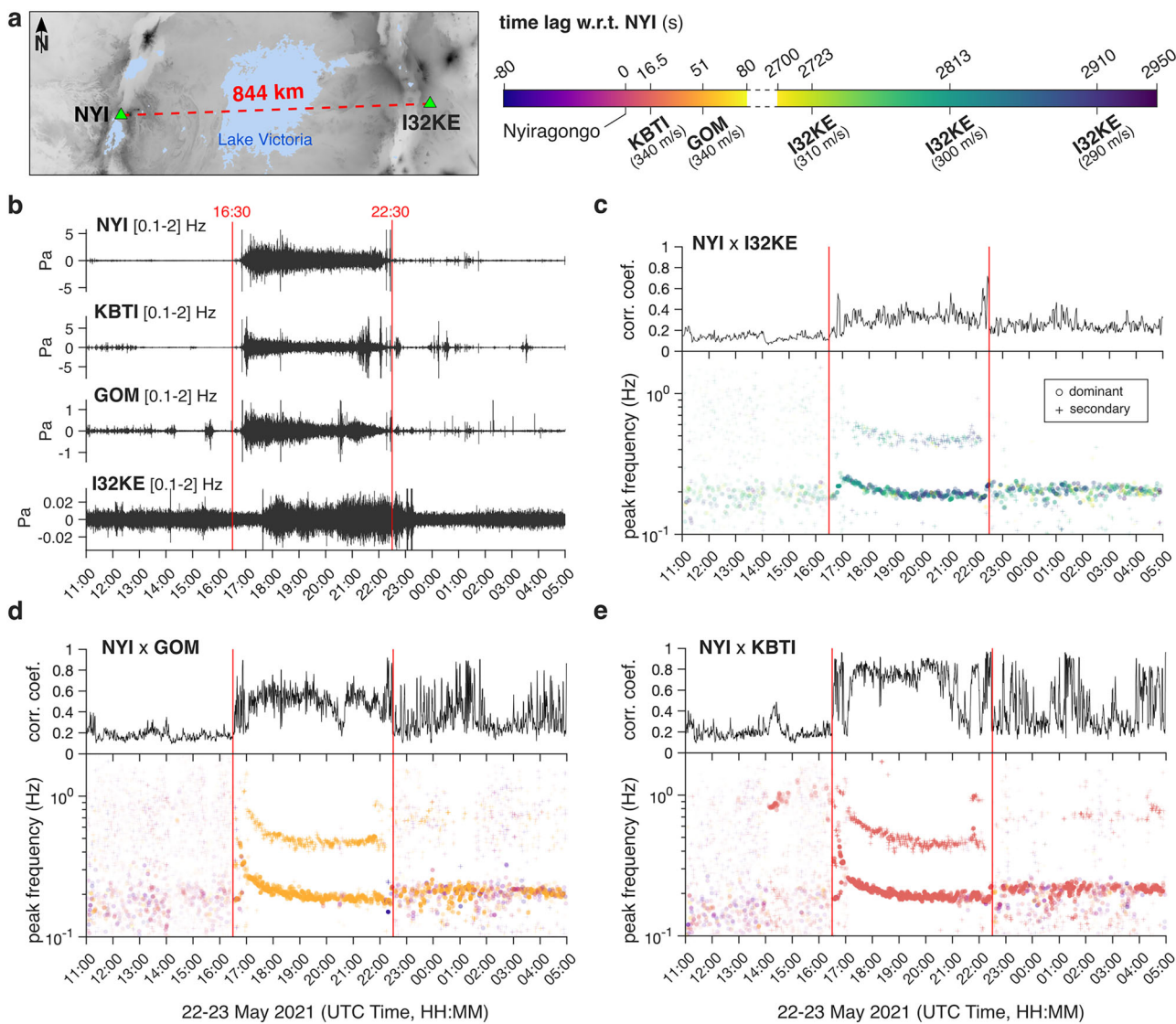


Fig. 3 | Infrasound peak frequencies from cross-correlated records. **a** Left, location map of Lake Victoria (blue area in the middle), the Nyiragongo volcano (pinned by its summit station NYI), and the infrasound station I32KE on the EAR's eastern branch. Right, color scale representing the time lag at KBTI, GOM, and I32KE with regards to an infrasound source at Nyiragongo (i.e., NYI) assuming direct propagation path and different apparent velocities (340 m/s for local stations, 290–310 m/s

for I32KE). **b** Infrasound records filtered between 0.1 and 2 Hz at all stations between 11:00 on 22 May and 05:00 on 23 May. Red lines (16:30–22:30) indicate the time interval associated with high amplitude in time domain and gliding dominant frequency and high correlation coefficients between NYI and I32KE (**c**) GOM (**d**) and KBTI (**e**). Note that NYI is used as reference providing a similar time stamp for correlation coefficients and peak frequencies between NYI and other stations.

16:30 and 17:20. There was no resonance when the lava lake was filled, so we have no clear point in time for the beginning of the drainage. However, both the sharp increase in infrasonic amplitude (Figs. 2 and 3) and the extrapolation of the lava-lake level models before 16:45 (Fig. 4), while assuming constant flush rate, point toward 16:30–16:35. Our result also suggests that the widening of the crater occurred rapidly during the same timeframe, though the uncertainty for this parameter is greater. The deepening of the lava-lake level remains the main factor controlling the decreasing frequency content of the infrasound harmonic tremor. According to our models, the crater floor collapsed after the full drainage of lava after 17:20 (~300 m), which corresponds to the moment where the deepening slowed down. After 19:00, the pit crater depth estimated around 380–390 m did not evolve much. This depth is close to the SAR-based estimate on 23 May at 04:03 (365 m)⁶⁵. Several large transient infrasound signals characterize the end of the eruption signal right before 22:30 (Supplementary Fig. S3). The sporadic tremor signature after 22:30 then exhibits a slight, but noticeable higher peak frequency nearly constant around 0.21 Hz and the loss of the first overtone with an overall decreasing signal amplitude (Fig. 3). The filling of the bottom

crater due to collapsing walls can explain this frequency change but the observed rise is minor and partly contained within the uncertainty of the models (Supplementary Fig. S11). These final infrasound transients, together with synchronous broadband seismic signals (Figs. 1, 2 and Supplementary Fig. S3), are thus likely coinciding with explosions or collapses that marginally changed the pit-crater geometry at that time, which remained stable up to the next satellite transit on 23 May at 04:03.

The complete scenario of the flank eruption

To understand the link between surface manifestations within the crater and along the flank of the volcano, infrasound can be used to track fissures opening and lava flows¹¹. At KBTI, an array of three operational infrasound sensors allows to compute the Direction of Arrival (DOA in °N) of infrasound signals during the eruption (Methods). Potential sources (main crater *Cr*, eruptive fissures *F1–F4*) are in line-of-sight with the station, with low incident angles (<15°). Arrivals from the main crater (*Cr*) may span an angular aperture of up to 16°, overlapping with potential sources from the highest fissure *F1*. In contrast with the low

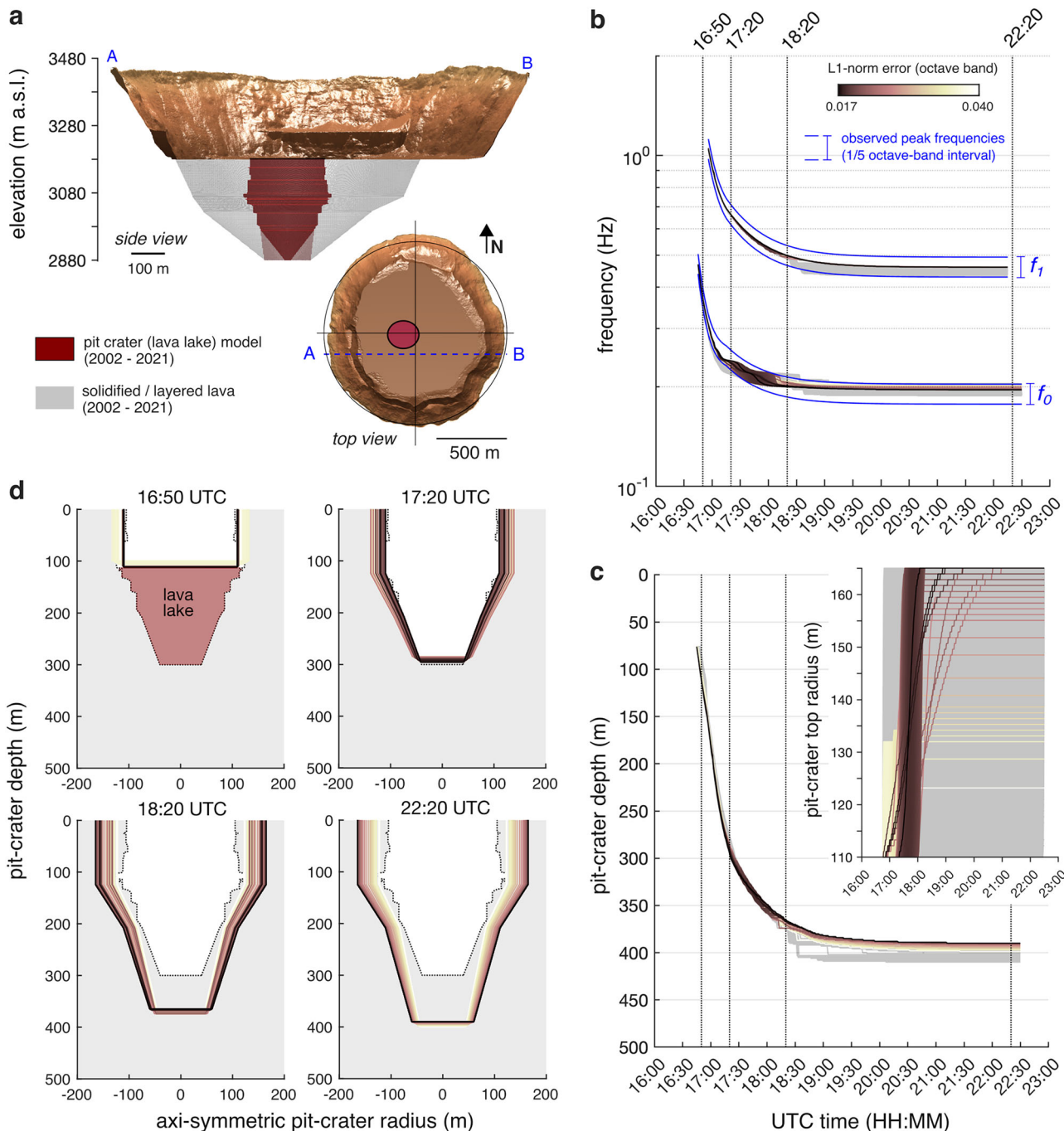


Fig. 4 | Time-varying acoustic resonance model of Nyiragongo's pit crater.

A Nyiragongo's cross-section model on 22 May 2021 before the eruption obtained from UAV-based photogrammetry model (DEM as brown surface) and from SAR-based amplitude images²⁸. Note that the diameter of the pit crater hosting the lava lake is poorly constrained below ~3.000 m a.s.l., that is along the last ~100 m of depth (bottom radii of 70 or 10 m are both represented). **b** Top, best-fit models of dominant (f_0) and secondary (f_1) peak frequencies. Observations are given as 1/5 octave-band intervals (blue lines) encompassing the range of observed peak frequencies. Models

are colored according to misfit (L1-norm) expressed in octave band. Models in gray are the ones going over the 1/5 octave band interval (blue lines). **c** Inverted pit-crater depth and top radius (inset) models corresponding to f_0 and f_1 models plotted above. **d** Pit-crater cross-sections corresponding to model estimates (i.e., crater's part not filled by lava) at 16:50, 17:20, 18:20, and 22:20 (vertical black dashed lines in **b**, **c**) plotted on the lava-lake extent (i.e., fully filled) estimated before the eruption (dotted lines). The inverted pit-crater models are colored according to the color code used in **(b, c)**.

frequency content of the intra-crater harmonic tremor mostly below 1 Hz, we analyse here signals within the range 1–8 Hz. This choice is driven by the array aperture for resolving accurate DOA¹⁷ but also corresponds to the high-frequency signals emitted during the eruption that differ from the harmonic tremor (Supplementary Fig. S3). Amplitude time-series at NYI, KBTI, and GOM filtered in this frequency band clearly show higher amplitude at KBTI between 17:00 and 19:00, thus

suggesting nearby sources of infrasound (Supplementary Fig. S13). After processing (Methods and Supplementary Figs. S15–19), the relevant parts of the recording are matched to the individual lava flows based on the estimated DOA (Fig. 5). The detected sources are most likely constrained to the vicinity of the eruptive fissures (F_1 to F_4) where the most powerful signals are generated during fissure opening and lava fountaining, as observed at Kilauea¹¹ or in Iceland⁷². However, infrasound

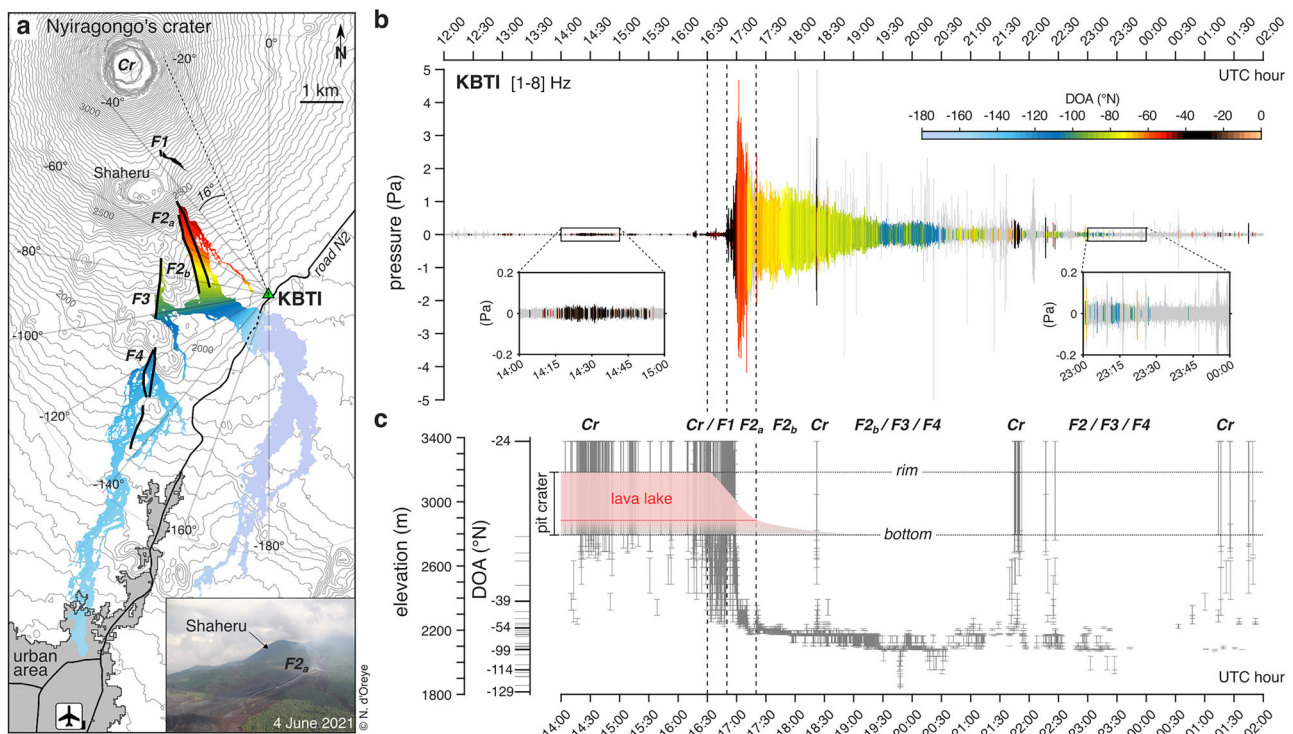


Fig. 5 | Tracking of lava eruptions on the flank compared with the drainage of the lava lake. **a**, Map of Nyiragongo's flank from the northern limit of the urban area (in gray) including the airport to the south, up to Nyiragongo's summit crater to the north. The background topography (contour lines) is derived from SRTM data with 1 arc-second resolution (NASA/USGS). The abbreviation *Cr* denotes Nyiragongo's crater and the main eruptive fissures are numbered *F1*, *F2_{a,b}*, *F3*, and *F4* from highest to lowest elevations, respectively. A picture taken from a helicopter on 4 June 2021 shows the Shaheru adventive crater and the fissure *F2_a* (inset). The lava flows are colored (from blue to red) according to the DOA (°N) with respect to KBTI station (green triangle). Intra-crater activity (*CR*) and *F1* corresponds to DOA colored in

black. Considering the location of eruptive fissures, DOA that do not correspond to potential eruptive sources are colored in light blue/magenta and light brown. The corresponding color scale is plotted in **(b)**. **b**, Infrasound record at KBTI colored according to DOA. Vertical dashed lines indicate 16:30, 16:50, and 17:20. **c**, Observed DOA converted into elevation along the fissures axe from Nyiragongo's crater to *F4* plotted as error bars. The drainage of the lava lake contained within the summit pit-crater is reproduced from Fig. 4 as the transparent red-to-gray area limited by the pit-crater rim on top and the maximum depth of the pit crater after the eruption on bottom.

from high-speed lava flow, such as produced by Nyiragongo (>10 m/s)⁷³, could also be recorded, as evidenced at Kilauea⁷⁴.

The DOA, being calculated by assuming source points coincide with the topography (see “Methods”), can be converted to elevation points of a topographic profile passing through the main eruptive fissures (Fig. 5 and Supplementary Fig. S20). This allows a direct comparison with the time-varying depth of the pit crater. The synchronicity of the lava-lake drainage with the successive opening of fissures from north (i.e., near the summit) to west (i.e., lower part of the flank) is obvious. The chronology of the flank eruption is deduced as follows (Fig. 5 and Supplementary Fig. S19):

- 1) Hours to minutes before the first signs of the seismic unrest at 15:57, the persistent lava lake acoustic signature from the crater (*CR*) is detected at the station, as for any other days in the years preceding the eruption¹⁷.
- 2) Between 15:57 and 16:50, signals with DOA spreading over ~20° toward the crater (*Cr*) associated with the beginning of the seismic crisis still have low amplitudes between 10^{-2} and 10^{-1} Pa commonly recorded during “quiescent” period¹⁷. Some clear impulsive signals with peak amplitude exceeding 10^{-1} Pa are detected, which may reflect a vigorous spattering activity of the lava lake.
- 3) A sharp amplitude increase around 16:50 may convey the first lava fountaining episodes from *F1* but also intense intra-crater activity (e.g., lava lake drainage, explosions/degassing).
- 4) A clear drift of the DOAs starting after 16:55 is associated with the paroxysmal phase of the lava fountaining along the fissure *F2_a* lasting about 15 min up to 17:10 characterized by maximum signal amplitude of a few Pa. By around 17:20, the paroxysm of the lava fountaining,

associated to the signal amplitude burst at KBTI starting at 16:50, was ending.

- 5) The following 10 min mark another drift of DOAs to the south that could be associated with fissures *F2_b* at the downstream level. Note that, at that time, many time-segments are not associated with DOAs because solutions can only be found for high apparent velocity (>400 m/s) in contradiction with straight-line propagation at local distance. Atmospheric effects and limited resolution in time and space from the three-element small aperture array are the most likely explanations (see “Methods” and Supplementary Figs. S18, S19).
- 6) Lava fountain activity persists along *F2* and potentially overlaps with *F3* for approximately the next two hours, up to 19:00. High amplitude impulsive signals coming from the crater are also detected around 18:20, which corresponds to the moment when the pit crater stabilized near its final depth. Amplitude at the tail of the eruptive signal continuously decreases, ending with signals from fissures *F3* and *F4* after 19:00. At that time, amplitudes at KBTI reach comparable lower levels recorded at NYI (Supplementary Fig. S13), which both support the overall energy decrease of the infrasound sources and their increasing distance to KBTI. Spurious arrivals from the overall fractured area persist during the following hours. Background signal amplitudes get closer to pre-eruptive level after 22:30 (see insets in Fig. 5b).

The exact start time at which lava appeared on the flank remains elusive due to DOA uncertainties. Based on our acoustic model, the lava lake level started to decrease around 16:30, which also marked a change in DOA from the main crater. However, the clearest drift with increase of infrasound

amplitude appears 20–25 min later, which coincides roughly with the first visual accounts of lava on the flank³⁵. Another 30 min later, the lava contained within the lake was completely flushed.

Toward a further understanding of Nyiragongo's lava-lake system

Like for other long-lived lava lakes⁷⁵, a stable feeding conduit connected to the bottom of the lava lake is expected. The infrasound-based results (Fig. 5) strongly suggest that a gravity-driven flow from the lava lake occurred through the vertical feeding conduit, then erupted along the flank fissures less than one hour after the start of the seismic unrest detected at NYI (i.e., 15:57). The analysis of seismicity can bring further evidence of the movement of magma from the central crater to the eruptive fissures through the lateral dyke crossing the edifice. Seismic events were detected and located between the crater and the eruptive fissures during the first hour of the eruptive unrest (i.e., ~16:00 to 17:00)³⁵ (Fig. 1a), though the dyke propagation becomes clearer outside the edifice (i.e., below KBTI's latitude) with swarm-like episodes of minor to moderate magnitude earthquakes. The comparative analysis of continuous amplitude time-series between NYI and KBTI in the band 0.333–15 Hz (Fig. 1b) can be used to infer magma movement within the edifice without the need of detecting/locating earthquakes⁴². Ignoring path or site effects on the recorded amplitude for the sake of simplicity^{42,76,77}, the qualitative analysis of seismic amplitude ratio indicates toward which station seismicity tends to migrate if sufficient seismic energy is radiated and detected at the considered stations. The amplitude ratio KBTI/NYI (Supplementary Fig. S14) clearly conveys the starting seismic unrest detected first at NYI (decrease of ratio) and the progressively higher amplitude increase at KBTI than at NYI (increase of ratio). The increasing trend of the ratio KBTI/NYI cannot be due to a shutdown of a source at the crater and a return to the pre-eruptive state because both summit (NYI) and flank (KBTI) seismic amplitude increase following the start of the unrest. Thus, this result is most likely the signature of a seismic disturbance first localized close the central crater, then followed by the migration of seismicity toward its southern flank.

Regarding the timing of this intrusive process, lava eruption from the highest eruptive fissure *F1*, which is located about 2000 m away from the lava lake (Supplementary Fig. S20), occurred less than 60 min after the start of seismic unrest at 15:57. From the analysis of the seismic amplitude ratio KBTI/NYI (Supplementary Fig. S13), the migration of seismicity toward the south becomes clearer after 16:15 (i.e., ~40 min before the flank eruption), which corresponds to the timing of the first seismic events detected across the local seismic network³⁵. According to our acoustic model, the lava-lake level did not fluctuate significantly before 16:30. If we consider the magma started to migrate from the main crater synchronously with the drainage of the lava lake, it would have taken only 25 min to reach the flank. Using this range of plausible travel times (i.e., between 25 and 60 min), we obtain dyke propagation velocities ranging between 0.55 and 1.33 m/s from the lava lake toward *F1*. These numbers are in accordance with observations of dyke intrusions at Piton de la Fournaise (La Réunion Island)⁷⁸ or in Iceland⁷⁹. Over the first 8 h since 16:00 UTC, according to seismicity (see dashed line “23 May” in Fig. 1a), the dyke progressed by about 10 km corresponding to an average velocity of ~1.25 km/h (i.e., below 0.5 m/s).

The estimated erupted volume³⁵ of lava was 10–15 Mm³ while the pre-eruptive lava lake volume²⁸ was estimated to be ~8 Mm³. To explain this discrepancy, an additional magma supply from depth is expected. This hypothesis is supported by the presence of primitive olivine in 2021 lava flows in notable proportion^{35,38} and the efficient hydraulic connection between the shallow and deepest part of the plumbing system^{28,32,40}. Regarding the shallowest contribution to the lava flows from the lava-lake system, knowing the pit-crater geometry and the time-varying lava-lake level (Fig. 4), we can estimate the downward flow rate through the eruptive fissures. We obtain a maximum volumetric flow rate of ~3000 m³/s (see “Methods”). To accommodate a flow rate of ~3000 m³/s, the width of the dyke idealized as a rectangular structure⁸⁰ should vary between 0.6 and 1.2 m (see “Methods”). These values are in accordance with the geometry of the

dyke below the edifice inverted from space geodesy (InSAR) observations³⁵ and within the typical range of dyke dimensions found in continental rift settings, like in Iceland⁸⁰. Increasing the dyke's extent at depth beneath the edifice down to 2000 m, according to the plausible range obtained from the InSAR-based dyke model, implies that the opening could be even narrower (i.e., less than 0.5 m). Thus, the observed flow rate during the lava-lake drainage was likely controlled by the dimensions of the vertical feeding conduit.

As a strong but necessary simplification, cylindrical conduit's dimensions (diameter and length) can be considered and expressed as a function of volumetric flow rate using well-established fluid flow models, such as the Hagen–Poiseuille law for laminar flow⁸¹ and the Darcy–Weisbach empirical relation for turbulent flow⁸². The assumption of a gravity-driven flow in a vertical conduit implies that the influence of the conduit length on the observed flow rate can be neglected⁸² (see “Methods”), contrary to conduit models where horizontal magma flow is also considered, e.g., from the central crater to the flank^{81,83}. Using the Darcy–Weisbach equation, Burgi and co-authors⁸² established that a conduit diameter of 15 m best explained the visual testimony of a 25-m drop of Nyiragongo's lava-lake level in 2011. Nevertheless, the measurement of the drop duration was not precise enough (less than 1 up to 5 min)^{30,82} to give a well constrained estimate (values of 7.5, 10, 12.5 and 15 m were tested). The flow rate derived from infrasound might bring more constraints because the timing of the drop is obtained from an acoustic numerical model reproducing well the resonant frequencies of the observed harmonic infrasound tremor. However, because they rely on indirect observations of the lava-lake level drop, such new estimates would still need to be further confirmed by other observations. Following Burgi and co-authors⁸² using the Darcy–Weisbach equation and conservative experimental/empirical values for Nyiragongo's magma properties, we obtain diameters of the shallow conduit ranging between 5 and 9 m (see “Methods”). These values are realistic bounds in agreement with modeling estimates reported at other lava lake volcanoes, Kilauea^{63,64}, Erebus (Antarctica)^{84,85} or Ambrym (Vanuatu)⁸⁶.

Four months after the flank eruption, lava reappeared in the summit crater, and a new lava lake has been forming since then, well detected on seismic⁴² and infrasound¹⁷ recordings. Further investigations of the available seismo-acoustic records, such as waveform inversion for the source mechanisms of seismic VLP events⁸⁷, are necessary to deepen our understanding of Nyiragongo's behavior and architecture. From a monitoring perspective, while recording seismicity potentially allows for the detection of abnormal signals shortly (~min to hour) before flank eruptions^{35,42} (Fig. 2), like at Piton de la Fournaise⁸⁸ or in Iceland⁸⁹, analyzing the infrasound signature can provide timely information in time and space about the eruptive processes, aiding in assessing the level of unrest. This study, being part of a long-term (2013–2022) ground-based monitoring initiative^{17,18,28,32,33,35,42,46,90,91}, promotes the development of infrasound measurements as a primary monitoring tool for Nyiragongo, despite recurrent socio-political issues and armed conflicts in the Kivu region. It also supports, in line with the most recent research in this field⁹², the development of similar approaches to other volcanoes worldwide.

Methods

Seismic and infrasound amplitude time series of local stations

As part of the KivuSNet seismic network (2013–2022)⁹⁰, seismometers deployed at NYI, KBTI, and GOM are 3-component broadband seismometers with a corner period of 120 s at NYI (Nanometric Trillium Compact posthole), KBTI (Nanometric Trillium Compact), and 60 s at GOM (Güralp CMG-3ESPC). The co-located infrasound sensors are infraBSU instruments (corner frequency of 10 s) manufactured by Boise State University⁴². One acoustic sensor is deployed at NYI, while three sensors are deployed at GOM and KBTI. Only one sensor for KBTI and GOM is used for computing CCFs (Fig. 3), which is chosen as the one providing the best CCFs' SNR (signal-to-noise ratio)³⁵.

The sampling rate for all instruments is 50 Hz. Root mean square (RMS) amplitude timeseries (Figs. 1 and 2) are computed from records

corrected for the instrumental response and filtered using zero-phase 4th-order Butterworth bandpass filter. RMS estimates are calculated over 1-min windows with 50% overlap (i.e., step every 30 s). For each time increment, moving average over centered 5-min windows are then computed. Zooming into seismo-acoustic events (Supplementary Figs. 4 and 5) is done after applying gain correction only (i.e., no deconvolution) and single pass (i.e., causal) 4th-order Butterworth bandpass filter.

Cross-correlation of infrasound records

The cross-correlation procedure is summarized as follows: (1) Raw data are filtered between 0.1 and 2 Hz and downsampled to 10 Hz; (2) Cross-correlation functions (CCFs) are calculated from successive 150-s signal segments with 75% overlap (i.e., step every 37.5 s). For the cross-correlation between NYI and I32KE, the I32KE trace is shifted by -2809s beforehand, which corresponds to the time shift observed for the first clear coherent infrasound event recorded at both stations at the start of the eruption. (3) CCFs provide values of correlation coefficients (CCFs amplitude) with respect to (negative and positive) time lag between both records. For each time segment, a coherent acoustic wave is likely to be detected across the station pair if the corresponding normalized CCF has a clear local maximum above 0.5 (for a range between 0 and 1). Maxima of each sliding CCFs are plotted in Fig. 3. This allows us to easily infer when coherent waves recorded at the summit (NYI) are also recorded at other stations. (4) The Fourier transform of CCF is the so-called cross-spectrum which allows for the identification of coherent frequencies between both records. The time-varying frequency changes of CCFs can be estimated by calculating the corresponding spectrogram (Short-Time Fourier Transform, STFT)⁹³. Similarly, we use the Continuous Wavelet Transform (CWT) to get the time-frequency distribution of CCFs. The STFT uses a fixed size for the sliding analyzing window that cannot be equally appropriated for every frequency component, which means a compromise must be found between time and frequency resolution. The CWT allows a more flexible 2D time-frequency resolution than STFT by convolving the 1D signal (i.e., the CCF) with scaled and translated versions of a mother wavelet (here a standard Morlet wavelet is used). From 2D time-frequency representation of each CCF, we extract the “local spectrum” corresponding to the time lag for which the correlation between both signals is maximized in order to retrieve the dominant and secondary frequency peaks. This procedure is summarized in Supplementary Fig. S10 and the results are plotted in Fig. 3. We observe that the local CWT or STFT spectra can be considered as a smoothed version of the standard cross-spectrum. Both CWT and STFT allow to identify unambiguously the same dominant and secondary frequency peaks but the prominence of the secondary peak is clearer with the CWT.

Crater acoustic resonance modeling

We used the CRes numerical model⁶⁷ to simulate infrasound signals during the drainage of the lava lake. Cres uses a 1D finite-difference frequency-domain method to compute the acoustic response function for an axisymmetric crater, which includes the crater acoustic response function (wave propagation inside the crater) and the atmosphere response function (acoustic radiation from the crater outlet to the receiver).

As shown in Fig. 3 and Supplementary Fig. S3, the infrasound signal is a harmonic tremor (i.e., continuous pressure perturbation), of which the fundamental frequency and the first overtone are clearly detected at local and distant stations. The simple approximation of isotropic radiation into a half space appears sufficient in our case for retrieving these frequency attributes from the simulated infrasound waveforms. The distance and/or altitude of the virtual receiver with regard to the crater outlet will not have any effect on the retrieved resonant frequencies, contrary to the pressure level⁹⁴. As suggested by Johnson and co-authors¹⁶, a baffled piston model is used at the crater outlet instead of an isotropic monopole source that radiates back into the crater and only valid for compact source dimensions, i.e., where $ka \ll 1$ with k the wavenumber and a the crater radius⁶⁷. Models including anisotropic radiation patterns, nonlinear propagation effects,

topography, winds, and atmosphere structure must be considered in order to better constrain eruption properties (e.g., volume of erupted material) derived from infrasound waveforms⁹⁴. In our case, we do not need to consider complex path effects because we do not analyze waveforms and amplitude of explosion signals at various distances and azimuth from the vent.

We also acknowledge that the chosen source models (Gauss or Brune models are available in CRes) play a role on the simulated frequency spectra⁶⁶. However, we can reasonably assume that the source has sufficient energy over a large frequency range for exciting the resonant modes in line with our observations. Thus, we do not need to know in detail the source mechanisms for explaining the resonant frequencies, which are mainly modulated by the crater geometry. As pointed out by Watson and co-authors⁶⁶ at Etna volcano, it is impossible to model the full complexity of the infrasound sources, which cannot be considered as a single discrete process but are rather the result of the sum of discrete processes over time generating continuous pressure perturbations. Therefore, it is unavoidable to simplify the source mechanism as a constant process that can be repeated over time, thus simulating the observed continuous signals. The volume flux source time function at the base of the crater is modeled as a Gaussian pulse with standard deviation of 0.15 s (Supplementary Fig. S11) in line with parameters set up by Johnson and co-authors¹⁶ for Villarica’s lava lake.

Aside from the crater geometry, the temperature and gas composition also modify the acoustic impedance, and thus the crater resonance. Because of the difficulty to estimate such parameters, standard values must be chosen. Atmosphere temperatures of 300–360 K (~ 27 –97 °C) above the lava lake were reported²⁶. Variations of less than 100 °C will have very limited influence on the final resonant frequencies⁶⁷. Similarly, variations in gas species would reduce the sound of speed by only 10% and have little impact on the resultant resonant frequencies⁶⁷. Hence, for modeling simplicity, we chose reasonable values applicable to both crater and atmosphere parts: 5 °C for the temperature and 1 kg/m³ for the gas density. Assuming dry air composition⁶⁷, the resultant speed of sound would be 334 m/s. Therefore, only the crater geometry will play a role in modifying the harmonic properties of the modeled infrasound records.

Resonant frequencies inversion for time-varying crater geometry

Data to invert are selected from Fig. 3. We keep the best estimates of resonant frequencies for station pair NYIxKBTI and NYIxGOM, of which maximum CCF’s coefficients exceed 0.5 for time delays corresponding to signals originating from Nyiragongo within an interval of ± 1.5 s around theoretical delay times (assuming straight-line wave propagation and velocity of 340 m/s). After a resampling to one data point per minute and per station pair, the selected data for the dominant (fundamental) and secondary (first overtone) frequencies are plotted in Supplementary Fig. S12. Best-fit models for f_0 and f_1 are computed, on the form $f = a + (b - a) * 10^{(-k.*t)}$ with f the frequency, t the time, a , b and k real positive numbers. Centered intervals of 1/5 octave band around the best-fit models encompass 91% and 87% of peak frequencies for f_0 and f_1 , respectively. Hence, we consider the best-fit models and the corresponding 1/5 octave intervals as final robust datasets to be inverted. The selected period for f_0 observations ranges from 16:45 to 22:30 and for f_1 observations from 16:55 to 22:15. Note that there is a slight increase of f_0 after 22:30 up to a value of around 0.208 Hz for the next few hours.

As a priori information about the crater geometry, we know the evolution of the mean crater radius over time between 2006 and 2021²⁸, allowing us to start with important constraints about the pit crater shape at the beginning of the eruption (Fig. 4). This complex shape is further simplified as a stack of 3 blocks made of, from top to bottom, one cylinder and two truncated inverted cones (i.e., decreasing radius with depth). From SAR images in Fig. 2, the mean top radius ranges from 110 m (value estimated before the eruption at 15:37 on 22 May) to 165 m (value estimated after the eruption at 04:03 on 23 May)⁶⁵. The bottom radius is not well-constrained. Values between 10 and 70 m would be acceptable in accordance with the pit-crater model²⁸ plotted in Fig. 4. We choose a mean bottom radius of 40 m.

The methodological inversion approach consists in computing resonant frequencies for a wide range of potential crater geometries. The free model parameters are the depth D (ranging from 15 to 500 m) and the width factor W of the crater (ranging between 1 and 1.5). The width factor W is applied uniformly to the three blocks, which implies that the top radius of the pit crater can increase from 110 to 165 and the bottom radius can increase from 40 to 60 m. For all potential values of D and W , we compute the difference between observed and simulated f_0 and f_1 in terms of octave band. Both residuals are averaged (i.e., f_0 and f_1 have the same weight) to get a final 3D matrix R of size [length(t), length(W), length(D)]. Before 16:55 and after 22:15, only f_0 observations are used. Because the crater radius can only stabilize or increase with time, we further assume that the evolution of the width factor W can be approximated by pre-defined sigmoid time functions $W(t) = 0.5 * (1 + \text{erf}[(t - \mu)/(\sigma\sqrt{2})])$ with erf the error function, x the number of time steps, σ the standard deviation and μ the mean of the considered temporal distribution, always starting with $W = 1$ (top radius = 110 m) and with final values ranging between 1 and 1.5 (top radius between 110 and 165 m). This function, known as cumulative distributive function of the normal distribution in the context of probability theory, allows to define realistic models for the time evolution of the crater width W by varying μ and σ . For all time-varying models of W , we look for the depth values D in the matrix R that give the lowest misfit with the additional constraint that D can only stabilize or increase after each time step t , since both observed f_0 and f_1 stabilize or decrease with time.

To summarize, we generate n sigmoid functions $W_n(t)$ obtained from n combinations of μ and σ . Thus, for each $W_n(t)$ function, we perform an incremental search for the depth function $D_n(t)$ that gives the lowest misfit at each time step between observed and computed resonant frequencies (with the constraint that $D_n(t) \geq D_n(t-1)$). This leads to 194,106 solutions, among which 23,913 models fall within the 1/5 octave intervals for both f_0 and f_1 . These numbers can be reduced to 1029 and 257 solutions respectively (see gray and colored models in Fig. 4), after removing nearly identical models defined as models with less than 2% of variations for any depth values (i.e., maximum of 10 m for $D = 500$ m) and 3% for any width values (i.e., maximum of 4.95 m for $W = 1.5$, which corresponds to a top radius of 165 m).

Infrasound arrays processing

KBTI is equipped with three sensors (infraBSU like the one deployed at NYI and GOM). They are connected to the same acquisition system (Nanometrics Centaur) with a small aperture of ~20-m between sensors³⁵, like other local deployments at volcanoes^{95,96}. Deploying at least three sensors at the same site allows performing array processing for retrieving the direction of arrival (DOA) and an apparent velocity (V_{app}) of coherent waves passing through the array. Based on the array response¹⁷, this deployment is efficient at detecting coherent infrasound arrivals in the frequency range 1–8 Hz. Standard least squares beamforming¹² can be applied to each 3-element array for successive windows of 10-s length overlapped by 50% to get DOA and V_{app} (Supplementary Fig. S15–18). Potential sources (crater, eruptive fissures) are in line-of-sight with the station with low incident angles (<15°) (Fig. 5 and Supplementary Figs. S6, 7, 20). We can thus assume subhorizontal plane wave propagation to the sensor array with apparent velocity close to the adiabatic sound speed ($V_{\text{app}} \sim 340$ m/s). Arrivals from the main crater may cover an angle aperture up to 16°, which overlaps with potential sources from the most elevated fissure F_1 . The determination of DOA can be largely affected by seasonal and daily variations within the shallow atmospheric boundary layer affecting wave propagation path and amplitude due to changing temperature and wind conditions^{17,93} (Supplementary Figs. S15 and 16). Regarding the above-mentioned effects, the eruption on 22 May 2021 occurred during an unfavorable year and daily period where DOA estimates can be strongly biased (Supplementary Figs. S17 and S18).

With only three sensors, a least-squares fitting of observed time delays cannot provide statistical meaningful uncertainties⁹⁵. In the specific time-frame of the eruption, we thus apply a grid-search strategy for finding the

DOA of direct waves (Supplementary Fig. S19), which is more suited to estimate DOA errors from a three-element small aperture array^{95,96}. First, we resample both signals by a factor 10 using cubic interpolation before cross-correlation⁹⁵, because the precision to measurements of arrivals at each sensor is limited by the initial sampling rate (50 Hz). Then, three normalized CCFs are computed for 5-s signal windows at 1-s time step for the three station pairs. A mean of the CCFs maxima (MCCM, standing for Mean of Cross-Correlation Maxima) equal or superior to 0.6 indicates that a coherent acoustic wave is potentially passing through the array. We consider each grid point on a map as a potential local source. For each pair of stations, each grid point is associated to a set of modeled time lags after assuming straight-line wave propagation with incident angles <15° (including topography) and intrinsic sound speed ranging from 340 to 360 m/s. Using standard equations provided in CRes^{67,70} linking air temperature and sound speed, this range corresponds to realistic end members for the average air temperature above the lava flow paths (15–50 °C) before and during the flank eruption between potential sources along the flow paths and KBTI array (see Fig. 5). Using a similar grid-search approach, Johnson and Ronan⁹⁶ considered a unique value of 343 m/s for locating volcanic rockfalls. The heat transfer to the atmosphere by the erupting and cooling lava flows is a complex time-dependent process and we do not intent to (and cannot) provide precise estimates of the ambient air temperature above the lava flows. The range 15–50 °C was defined according to mean air temperatures in the Kivu between Goma and Nyiragongo's summit³⁷ and reported measurements of atmosphere temperature above Nyiragongo's and Erta Ale's lava lakes²⁶. This allows to consider conservative uncertainties about probable variations of the intrinsic sound speed velocity during the eruption. Grid points where time delays correspond to the maximum of the CCFs for this range of acceptable velocities are set to 1, otherwise 0. Three grids for three station pairs are then stacked. Hence, we obtain a final spatial grid with values ranging from 0 (no source) up to 3 if there is a source region satisfying all station-pair observations. Because of the geometry of the array with sensors close to each other, the source region looks like a narrow strip area extending from the station site. This means that only DOA can be resolved and not a specific point source in 2D space. Thus, for each sliding 5-s window, we retrieve the mean, minimum and maximum DOA of the identified source region (i.e., the one where grid values equal 3). In Fig. 5, the mean DOA over time is represented by the color code and the DOA range (minimum to maximum) is represented by the error bars.

Infrasound array I32KE in Nairobi, Kenya is part of the International Monitoring System (IMS) that is currently being installed for the verification of the Comprehensive Nuclear-Test-Ban Treaty (CTBT). I32KE consists of seven absolute MB3a microbarometers that form a 2 km aperture array. The array layout consists of a triangular outer structure enclosing a trapezoidal inner array. All microbarometers measure atmospheric pressure fluctuations through an 18-m aperture wind noise reduction system, each of which has 96 inlet ports. The array was originally installed in 2003 and was revalidated in 2019.

During the time of the eruption, element I32H1 was not operational; instead, six elements were used in this study. The processing of the array is carried out using a standard time-domain delay-and-sum beamformer. As an event detector, we evaluate the Fisher ratio for which a probability of detection can be evaluated under assumption of a given SNR^{93,98}.

The raw signals are detrended and filtered in a 0.4–3 Hz passband. The filtered signals are upsampled to 200 Hz and processed in 30 s windows with 95% overlap. For each window, the slowness that best aligns the signals is determined following a grid search method. The slowness grid is parameterized by the back azimuth and apparent phase speed values of interest. In this case, the back azimuth values vary between 253 and 281° in steps of 0.1°. Apparent phase speeds vary between 300–400 m/s in steps of 1 m/s.

Processing results are shown in Supplementary Fig. S8. I32KE's trace corresponds to the best beam with a back-azimuth of 267.4° (i.e., pointing toward Nyiragongo) and an apparent phase speed of 342 m/s. The best beam is computed in the frequency domain using the unfiltered, detrended signals; a wider frequency band is used to compute the spectrogram. Ray

tracing modeling^{99,100} results for propagation from Nyiragongo to Kenya given in Supplementary Fig. S9 and Supplementary Table S1 are in good agreement with observations (Fig. 3 and Supplementary Fig. S8).

Conduit diameter and dyke width

Regarding the vertical conduit, the Hagen-Poiseuille equation for laminar flow in a cylindrical tube gives:

$$Q = \frac{\pi \Delta P R^4}{8 \eta L}, \quad (1)$$

with Q the volumetric flow rate (m^3/s), ΔP the pressure gradient (Pa), R the conduit radius (m), η the fluid viscosity (Pa.s), and L the conduit length (m). ΔP can be expressed as $\Delta P = \rho g \Delta H$, with ρ the fluid density (kg/m^3), g the acceleration due to gravity (m/s^2) and the differential height $\Delta H = L + h$, with h the height of the lava lake. h is obtained by subtracting the inverted depth value (distance from the rim to the lava lake surface, Fig. 4) to the total height of the pit-crater before collapse (300 m). The conduit diameter D is thus expressed by:

$$D = 2 \sqrt[4]{\frac{8 \eta Q L}{\pi \rho g (L + h)}} \quad (2)$$

The time period used for estimating the mean flow rate Q is chosen according to 2 criteria: both f_0 and f_1 observations are available (i.e., after 16:55) and the geometry of the pit crater is well constrained (height of the lava lake above 90 m, i.e., before 17:03). We obtain $Q \sim 3000 \text{ m}^3/\text{s}$, $h = [94-155] \text{ m}$ and $L = [130-630] \text{ m}$ if the differential height between the bottom of the lava lake and the eruptive fissures is assumed to be representative of the conduit length L . As a reasonable simplification, the conduit length L and the height of the lava lake h can be neglected in Eq. (2) since “ L ” in numerator and “ $(L + h)$ ” in denominator are of the same order of magnitude. We thus obtain:

$$D \approx 2 \sqrt[4]{\frac{8 \eta Q}{\pi \rho g}} \quad (3)$$

Using experimental values^{73,101} of $\eta = 30-60 \text{ Pa.s}$ and $\rho = 2800 \text{ kg}/\text{m}^3$, Eq. (3) suggests that D would be around 3.4–4 m (close values around 2.8–3.9 are obtained using Eq. 2, $L = 130-630$ and $h = 94-155$). Taking into account other flow regimes that deviate from the laminar flow, the Darcy-Weisbach empirical equation can be considered⁸²:

$$Q = \pi D^{5/2} \sqrt{\frac{\Delta P}{8 f \rho L}} \quad (4)$$

From Eq. (4) and again neglecting the conduit length L and the height of the lava lake h , we get:

$$D \approx \sqrt[5]{\frac{8 f Q^2}{\pi^2 g}} \quad (5)$$

It introduces the dimensionless friction factor f that characterizes the resistance to flow due to friction. f is partly dependent on the conduit diameter and can be expressed through a variety of models depending on the flow regimes. For turbulent flow regime that corresponds to our situation (low viscosity magma above the fragmentation level characterized by high Reynolds number)^{82,102}, f becomes weakly dependent on the channel geometry and is more related to the roughness of the conduit walls¹⁰³, with experimental values ranging between 0.004 and 0.08 (Note that a factor 4 is applied between the definition of f by Mastin and Ghiorso¹⁰² and Wilson

and Head¹⁰³). At Nyiragongo, values between 0.02 and 0.06 were considered⁸². Thus, for a conservative range of f between 0.004 and 0.08, D would only vary between 4.9 and 9 m. As for the laminar flow, similar values (4.2–8.7) are obtained if we add the conduit length L and the height of the lava lake h to Eq. (5) in the expression of D .

To link the estimated flow rate derived from the drainage of the lava lake with the geometry of the vertical conduit, we have implicitly considered that the shallow dyke structure connecting the vertical conduit and the eruptive fissures can accommodate this flow rate. For a magma channel described as a rectangular dyke geometry, the flow rate is expressed as⁸⁰:

$$Q = \frac{\Delta P d w^3}{12 \eta l} \quad (6)$$

where d is the long-side length (extent at depth), w is the short-side length (opening of the dyke), and l is the length of the channel (lateral extent). In order to verify that realistic values of w are obtained for the inferred flow rate Q ($3000 \text{ m}^3/\text{s}$), we get:

$$w = \sqrt[3]{\frac{12 Q \eta l}{d \Delta P}} \quad (7)$$

We set d to 500 m in accordance with the extent of fissures F1/F2a (2250–2750 m a.s.l.) during the initial phase of lava flows between 16:55 and 17:03 (Fig. 5 and Supplementary Fig. S13). While the dyke was propagating toward the Lake Kivu at shallow depth (less than 500 m), d became much larger with a maximum extent of about 10–12 km beneath Goma³⁵. l is the lateral distance between the lava lake and the eruptive fissures on the flank that reached the Shaheru crater (i.e., Fissures F1/F2a), ranging approximately between 2000 and 3000 m. ΔP is the driving pressure depending on conditions at the two ends of the channel. Right beneath the lava lake, at depth corresponding to the extension of fissures F1/F2a observed on the flank, the magma-static pressure would vary between ~8 and 20 MPa. We thus obtain values of w varying between 0.6 and 1.2 m in order to accommodate a flow rate of $3000 \text{ m}^3/\text{s}$ during the drainage of the lava lake. Increasing the extent of d beneath the edifice at depth down to 2000 m, according to the plausible range obtained from the InSAR-based dyke model, leads to an opening of less than 0.5 m.

Data availability

Local infrasound and seismic data archiving and accessibility are ensured through the GEOFON program of the GFZ German Research Centre for Geosciences (<https://doi.org/10.14470/XI058335>) under the KV FDSN code (<http://www.fdsn.org/networks/detail/KV/>). For research purposes, infrasound data from the International Monitoring System are freely available through the CTBTO's virtual Data Exploitation Centre (vDEC <https://www.ctbto.org/specials/vdec/>) and can be requested online. COSMO-SkyMed data (ISA) are available from the Virunga Supersite Initiative (<https://geosnl.org/supersites/permanent-supersites/virunga-supersite/>). Source data for charts in Figs. 1–5 are available online at https://www.ecgs.lu/article-dataset/Dataset_BARRIERE_etal_2025_COMMSENV.zip.

Code availability

Data processing was performed under the MATLAB environment using built-in functions (e.g., filtering, STFT, CWT). CRes is available at <https://doi.org/10.5281/zenodo.6946566> and <https://github.com/leighton-watson/CRes>. The array processing of local infrasound records has been adapted from the software implementation of least-square beamforming provided by De Angelis et al.¹², available at <https://github.com/silvioda/Infrasound-Array-Processing-Matlab>. The beamforming code used for IMS data is available on <https://doi.org/10.5281/zenodo.10260259>. Model and ray tracer for propagation from Nyiragongo to Kenya are available at <https://doi.org/10.5281/zenodo.5562712> and <https://github.com/LANL-Seismoacoustics/infraGA>, respectively.

The AMSTer software is available at https://github.com/AMSTerUsers/AMSTer_Distribution.

Received: 26 March 2025; Accepted: 21 October 2025;

Published online: 27 November 2025

References

1. Valentine, G. A. & Gregg, T. K. P. Continental basaltic volcanoes – Processes and problems. *J. Volcanol. Geotherm. Res.* **177**, 857–873 (2008).
2. Chouet, B. A. & Matoza, R. S. A multi-decadal view of seismic methods for detecting precursors of magma movement and eruption. *J. Volcanol. Geotherm. Res.* **252**, 108–175 (2013).
3. Chouet, B. Volcano seismology. *Pure Appl. Geophys.* **160**, 739–788 (2003).
4. Witt, T. I. *Camera Monitoring at Volcanoes*. PhD Thesis, Universität Potsdam (2018).
5. Patrick, M. R., Orr, T. R., Swanson, D. A., Elias, T. & Shiro, B. *Lava Lake Activity at the Summit of Kilauea Volcano in 2016* (Scientific Investigations Report 2018–5008) <https://doi.org/10.3133/sir20185008> (2018).
6. Spampinato, L., Calvari, S., Oppenheimer, C. & Boschi, E. Volcano surveillance using infrared cameras. *Earth Sci. Rev.* **106**, 63–91 (2011).
7. Harris, A. *Thermal Remote Sensing of Active Volcanoes: A User's Manual* (Cambridge University Press, 2013).
8. Matoza, R., Fee, D., Green, D. & Mialle, P. Volcano infrasound and the international monitoring system. in *Infrasound Monitoring for Atmospheric Studies: Challenges in Middle Atmosphere Dynamics and Societal Benefits* (eds Le Pichon, A., Blanc, E. & Hauchecorne, A.) 1023–1077 (Springer International Publishing, 2019).
9. Johnson, J. Local Volcano Infrasound Monitoring BT. in *Infrasound Monitoring for Atmospheric Studies: Challenges in Middle Atmosphere Dynamics and Societal Benefits* (eds. Le Pichon, A., Blanc, E. & Hauchecorne, A.) 989–1022 (Springer International Publishing, Cham, 2019).
10. Fee, D. et al. Infrasonic harmonic tremor and degassing bursts from Halema'uma'u Crater, Kilauea Volcano, Hawaii. *J. Geophys. Res. Solid Earth* **115**, 1–15 (2010).
11. Thelen, W., Waite, G., Lyons, J. & Fee, D. Infrasound observations and constraints on the 2018 eruption of Kilauea Volcano, Hawaii. *Bull. Volcanol.* **84**, 76 (2022).
12. De Angelis, S. et al. Uncertainty in detection of volcanic activity using infrasound arrays: examples From Mt. Etna. *Italy Front. Earth Sci.* **8**, 1–11 (2020).
13. Cannata, A., Sciotto, M., Spampinato, L. & Spina, L. Insights into explosive activity at closely-spaced eruptive vents using infrasound signals: example of Mt. Etna 2008 eruption. *J. Volcanol. Geotherm. Res.* **208**, 1–11 (2011).
14. Ripepe, M., Delle Donne, D., Lacanna, G., Marchetti, E. & Ulivieri, G. The onset of the 2007 Stromboli effusive eruption recorded by an integrated geophysical network. *J. Volcanol. Geotherm. Res.* **182**, 131–136 (2009).
15. Ripepe, M., Marchetti, E. & Ulivieri, G. Infrasonic monitoring at Stromboli volcano during the 2003 effusive eruption: insights on the explosive and degassing process of an open conduit system. *J. Geophys. Res. Solid Earth* **112**, B09207 (2007).
16. Johnson, J. B., Watson, L. M., Palma, J. L., Dunham, E. M. & Anderson, J. F. Forecasting the eruption of an open-vent volcano using resonant infrasound tones. *Geophys. Res. Lett.* **45**, 2213–2220 (2018).
17. Barrière, J. et al. Local infrasound monitoring of lava eruptions at Nyiragongo Volcano (D.R. Congo) using urban and near-source stations. *Geophys. Res. Lett.* **50**, e2023GL104664 (2023).
18. Barrière, J. et al. Single-station seismo-acoustic monitoring of Nyiragongo's Lava Lake Activity, D.R. Congo. *Front. Earth Sci.* **6**, 82 (2018).
19. Fee, D. & Matoza, R. S. An overview of volcano infrasound: from Hawaiian to plinian, local to global. *J. Volcanol. Geotherm. Res.* **249**, 123–139 (2013).
20. Matoza, R. S. et al. Atmospheric waves and global seismoacoustic observations of the January 2022 Hunga eruption, Tonga. *Science* **377**, 95–100 (2022).
21. Matoza, R. S. et al. Long-range acoustic observations of the Eyjafjallajökull eruption, Iceland, April–May 2010. *Geophys. Res. Lett.* **38**, L06308 (2011).
22. Morelli, R. S., Gheri, D., Campus, P., Coppola, D. & Marchetti, E. Long range infrasound monitoring of Yasur volcano. *J. Volcanol. Geotherm. Res.* **432**, 107707 (2022).
23. Le Pichon, A. et al. Using dense seismo-acoustic network to provide timely warning of the 2019 paroxysmal Stromboli eruptions. *Sci. Rep.* **11**, 14464 (2021).
24. Marchetti, E. et al. Long range infrasound monitoring of Etna volcano. *Sci. Rep.* **9**, 1–10 (2019).
25. Garcés, M. et al. Infrasonic tremor observed at Kilauea Volcano, Hawai'i. *Geophys. Res. Lett.* **30**, <https://doi.org/10.1029/2003GL018038> (2003).
26. Valade, S., Ripepe, M., Giuffrida, G., Karume, K. & Tedesco, D. Dynamics of Mount Nyiragongo lava lake inferred from thermal imaging and infrasound array. *Earth Planet. Sci. Lett.* **500**, 192–204 (2018).
27. Wright, R., Blackett, M. & Hill-Butler, C. Some observations regarding the thermal flux from Earth's erupting volcanoes for the period of 2000 to 2014. *Geophys. Res. Lett.* **42**, 282–289 (2015).
28. Barrière, J. et al. Intra-crater eruption dynamics at Nyiragongo (D.R. Congo), 2002–2021. *J. Geophys. Res. Solid Earth* **127**, 2002–2021 (2022).
29. Sawyer, G., Carn, S. A., Tsanev, V. I., Oppenheimer, C. & Burton, M. Investigation into magma degassing at Nyiragongo volcano, Democratic Republic of the Congo. *Geochem. Geophys. Geosyst.* **9**, Q02017 (2008).
30. Bobrowski, N. et al. Multi-component gas emission measurements of the active lava lake of Nyiragongo, DR Congo. *J. Afr. Earth Sci.* **134**, 856–865 (2017).
31. Spampinato, L. et al. Thermal insights into the dynamics of Nyiragongo lava lake from ground and satellite measurements. *J. Geophys. Res. Solid Earth* **118**, 5771–5784 (2013).
32. Barrière, J. et al. Seismicity and outgassing dynamics of Nyiragongo volcano. *Earth Planet. Sci. Lett.* **528**, 115821 (2019).
33. Barrière, J., Oth, A., Theys, N., d'Oreye, N. & Kervyn, F. Long-term monitoring of long-period seismicity and space-based SO₂ observations at African lava lake volcanoes Nyiragongo and Nyamulagira (DR Congo). *Geophys. Res. Lett.* **44**, 6020–6029 (2017).
34. Arellano, S. et al. Long-term monitoring of SO₂ quiescent degassing from Nyiragongo's lava lake. *J. Afr. Earth Sci.* **134**, 866–873 (2017).
35. Smittarello, D. et al. Precursor-free eruption triggered by edifice rupture at Nyiragongo volcano. *Nature* **609**, 83–88 (2022).
36. Niu, J. Very-long-period signal reveals lava lake sloshing and its interaction with a deep reservoir in Nyiragongo volcano. *J. Volcanol. Geotherm. Res.* **450**, 108088 (2024).
37. Tanaka, K. Seismicity and focal mechanism of the volcanic earthquakes in the Virunga volcanic region. in *Volcanoes Nyiragongo and Nyamulagira: Geophysical Aspects* (ed. Hamaguchi, H.) 19–28 (Sendai, 1983).
38. Molendijk, S. M. et al. Plumbing system architecture and differentiation processes of the Nyiragongo Volcano, DR Congo. *J. Petrol.* **65**, egad088 (2024).

39. Demant, A., Lestrade, P., Lubala, R. T., Kampunzu, A. B. & Durieux, J. Volcanological and petrological evolution of Nyiragongo volcano, Virunga volcanic field, Zaire. *Bull. Volcanol.* **56**, 47–61 (1994).

40. Walwer, D. et al. Modeling the intermittent lava lake drops occurring between 2015 and 2021 at Nyiragongo Volcano. *Geophys. Res. Lett.* **50**, e2022GL102365 (2023).

41. Mafuko Nyandwi, B., Kervyn, M., Habiyaremye, F. M., Kervyn, F. & Michellier, C. Differences in volcanic risk perception among Goma's population before the Nyiragongo eruption of May 2021, Virunga volcanic province (DR Congo). *Nat. Hazards Earth Syst. Sci.* **23**, 933–953 (2023).

42. Subira, J. Seismicity and seismological models of the virunga volcanic province and Kivu Rift, Democratic Republic of Congo TT - Sismicité et Modèles Sismologiques dans la Province Volcanique de Virunga et dans le Rift du Kivu. PhD Thesis, Université de Liège (2024).

43. Hupe, P., Ceranna, L., Le Pichon, A., Matoza, R. S. & Mialle, P. International monitoring system infrasound data products for atmospheric studies and civilian applications. *Earth Syst. Sci. Data* **14**, 4201–4230 (2022).

44. Vergniolle, S. & Métrich, N. An interpretative view of open-vent volcanoes. *Bull. Volcano.* **84**, 83 (2022).

45. Acocella, V. et al. Towards scientific forecasting of magmatic eruptions. *Nat. Rev. Earth Environ.* **5**, 5–22 (2024).

46. Subira, J. et al. Detecting sources of shallow tremor at neighboring volcanoes in the Virunga Volcanic Province using seismic amplitude ratio analysis (SARA). *Bull. Volcanol.* **85**, 27 (2023).

47. Patrick, M. R. et al. Shallowly driven fluctuations in lava lake outgassing (gas pistonning), Kilauea Volcano. *Earth Planet. Sci. Lett.* **433**, 326–338 (2016).

48. Nadeau, P. A. et al. Using SO₂ camera imagery and seismicity to examine degassing and gas accumulation at Kilauea Volcano, May 2010. *J. Volcanol. Geotherm. Res.* **300**, 70–80 (2014).

49. Harris, A. J. L., Carniel, R. & Jones, J. Identification of variable convective regimes at Erta Ale Lava Lake. *J. Volcanol. Geotherm. Res.* **142**, 207–223 (2005).

50. Bouche, E. et al. The role of large bubbles detected from acoustic measurements on the dynamics of Erta'Ale lava lake (Ethiopia). *Earth Planet. Sci. Lett.* **295**, 37–48 (2010).

51. Richardson, J. P., Waite, G. P. & Palma, J. L. Varying seismic-acoustic properties of the fluctuating lava lake at Villarrica volcano, Chile. *J. Geophys. Res. Solid Earth* **119**, 5560–5573 (2014).

52. Ripepe, M. et al. Monochromatic infrasonic tremor driven by persistent degassing and convection at Villarrica Volcano, Chile. *Geophys. Res. Lett.* **37**, 2–7 (2010).

53. Bean, C. J. et al. Long-period seismicity in the shallow volcanic edifice formed from slow-rupture earthquakes. *Nat. Geosci.* **7**, 71–75 (2014).

54. Harrington, R. M. & Brodsky, E. E. Volcanic hybrid earthquakes that are brittle-failure events. *Geophys. Res. Lett.* **34**, L06308 (2007).

55. Ripepe, M., Delle Donne, D., Legrand, D., Valade, S. & Lacanna, G. Magma pressure discharge induces very long period seismicity. *Sci. Rep.* **11**, 20065 (2021).

56. Maeda, Y. & Takeo, M. Very-long-period pulses at Asama volcano, central Japan, inferred from dense seismic observations. *Geophys. J. Int.* **185**, 265–282 (2011).

57. Gudmundsson, M. T. et al. Gradual caldera collapse at Bárðarbunga volcano, Iceland, regulated by lateral magma outflow. *Science* **353**, aaf8988 (2016).

58. Fontaine, F. R. et al. Very- and ultra-long-period seismic signals prior to and during caldera formation on La Réunion Island. *Sci. Rep.* **9**, 8068 (2019).

59. Chouet, B. et al. Source mechanisms of explosions at Stromboli Volcano, Italy, determined from moment-tensor inversions of very-long-period data. *J. Geophys. Res. Solid Earth* **108**, 7–25 (2003).

60. Kumagai, H. et al. Very-long-period seismic signals and caldera formation at Miyake Island, Japan. *Science* **293**, 687–690 (2001).

61. Matoza, R. S. et al. High-rate very-long-period seismicity at Yasur volcano, Vanuatu: source mechanism and decoupling from surficial explosions and infrasound. *Geophys. J. Int.* **230**, 392–426 (2022).

62. Lyons, J. J. & Waite, G. P. Dynamics of explosive volcanism at Fuego volcano imaged with very long period seismicity. *J. Geophys. Res. Solid Earth* **116**, B09303 (2011).

63. Liang, C., Crozier, J., Karlstrom, L. & Dunham, E. M. Magma oscillations in a conduit-reservoir system, application to very long period (VLP) seismicity at basaltic volcanoes: 2. Data inversion and interpretation at Kilauea Volcano. *J. Geophys. Res. Solid Earth* **125**, 1–24 (2020).

64. Chouet, B. & Dawson, P. Very long period conduit oscillations induced by rockfalls at Kilauea Volcano, Hawaii. *J. Geophys. Res. Solid Earth* **118**, 5352–5371 (2013).

65. Smittarello, D. et al. Nyiragongo crater collapses measured by multi-sensor SAR amplitude time series. *J. Geophys. Res. Solid Earth* **128**, e2023JB026683 (2023).

66. Watson, L. M., Johnson, J. B., Sciotto, M. & Cannata, A. Changes in crater geometry revealed by inversion of harmonic infrasound observations: 24 December 2018 eruption of Mount Etna, Italy. *Geophys. Res. Lett.* **47**, e2020GL088077 (2020).

67. Watson, L. M., Dunham, E. M. & Johnson, J. B. Simulation and inversion of harmonic infrasound from open-vent volcanoes using an efficient quasi-1D crater model. *J. Volcanol. Geotherm. Res.* **380**, 64–79 (2019).

68. Johnson, J. B. et al. Infrasound tornillos produced by Volcán Cotopaxi's deep crater. *Geophys. Res. Lett.* **45**, 5436–5444 (2018).

69. Sciotto, M. et al. Infrasonic gliding reflects a rising magma column at Mount Etna (Italy). *Sci. Rep.* **12**, 16954 (2022).

70. Watson, L. leighton-watson/CRes: CRes (v1.1). Zenodo. <https://doi.org/10.5281/zenodo.6946566> (2022).

71. Jones, K. R., Johnson, J. B., Aster, R., Kyle, P. R. & McIntosh, W. C. Infrasonic tracking of large bubble bursts and ash venting at Erebus Volcano, Antarctica. *J. Volcanol. Geotherm. Res.* **177**, 661–672 (2008).

72. Lamb, O. D. et al. Acoustic observations of lava fountain activity during the 2021 Fagradalsfjall eruption, Iceland. *Bull. Volcano.* **84**, 96 (2022).

73. Morrison, A., Whittington, A., Smets, B., Kervyn, M. & Sehlke, A. The rheology of crystallizing basaltic lavas from Nyiragongo and Nyamuragira volcanoes, D.R.C. *Volcanica* **3**, 1–28 (2020).

74. Lyons, J. J., Dietterich, H. R., Patrick, M. P. & Fee, D. High-speed lava flow infrasound from Kilauea's fissure 8 and its utility in monitoring effusion rate. *Bull. Volcanol.* **83**, 66 (2021).

75. Lev, E. et al. A global synthesis of lava lake dynamics. *J. Volcanol. Geotherm. Res.* **381**, 16–31 (2019).

76. Caudron, C., Taisne, B., Kugaenko, Y. & Saltykov, V. Magma migration at the onset of the 2012–13 Tolbachik eruption revealed by seismic amplitude ratio analysis. *J. Volcanol. Geotherm. Res.* **307**, 60–67 (2015).

77. Tan, C. T., Taisne, B., Neuberg, J. & Basuki, A. Real-time assessment of potential seismic migration within a monitoring network using Red-flag SARA. *J. Volcanol. Geotherm. Res.* **384**, 31–47 (2019).

78. Peltier, A., Ferrazzini, V., Staudacher, T. & Bachéléry, P. Imaging the dynamics of dyke propagation prior to the 2000–2003 flank eruptions at Piton de la Fournaise, Réunion Island. *Geophys. Res. Lett.* **32**, 1–5 (2005).

79. Gudmundsson, A. The geometry and growth of dykes. in *Physics and Chemistry of Dykes* (eds Baer, G. & Heimann, A) (A A BALKEMA, 1995).

80. Sigmundsson, F. et al. Fracturing and tectonic stress drive ultrarapid magma flow into dikes. *Science* ((1979)) **383**, 1228–1235 (2024).

81. Ripepe, M. et al. Volcano seismicity and ground deformation unveil the gravity-driven magma discharge dynamics of a volcanic eruption. *Nat. Commun.* **6**, 6998 (2015).

82. Burgi, P. Y., Darrah, T. H., Tedesco, D. & Eymold, W. K. Dynamics of the Mount Nyiragongo lava lake. *J. Geophys. Res. Solid Earth* **119**, 4106–4122 (2014).

83. Patrick, M., Orr, T., Anderson, K. & Swanson, D. Eruptions in sync: improved constraints on Kilauea Volcano's hydraulic connection. *Earth Planet. Sci. Lett.* **507**, 50–61 (2019).

84. Calkins, J., Oppenheimer, C. & Kyle, P. R. Ground-based thermal imaging of lava lakes at Erebus volcano, Antarctica. *J. Volcanol. Geotherm. Res.* **177**, 695–704 (2008).

85. Molina, I., Burgisser, A. & Oppenheimer, C. Numerical simulations of convection in crystal-bearing magmas: a case study of the magmatic system at Erebus, Antarctica. *J. Geophys. Res. Solid Earth* **117**, B07209 (2012).

86. Allard, P., Burton, M., Sawyer, G. & Bani, P. Degassing dynamics of basaltic lava lake at a top-ranking volatile emitter: Ambrym volcano, Vanuatu arc. *Earth Planet. Sci. Lett.* **448**, 69–80 (2016).

87. Konstantinou, K. I. A review of the source characteristics and physical mechanisms of very long period (VLP) seismic signals at active volcanoes. *Surv. Geophys.* **45**, 117–149 (2024).

88. Roult, G. et al. A new comprehensive classification of the Piton de la Fournaise activity spanning the 1985–2010 period. Search and analysis of short-term precursors from a broad-band seismological station. *J. Volcanol. Geotherm. Res.* **241–242**, 78–104 (2012).

89. Einarsson, P. Short-term seismic precursors to Icelandic eruptions 1973–2014. *Front. Earth Sci.* **6**, 45 (2018).

90. Oth, A. et al. KivuSNet: the first dense broadband seismic network for the Kivu Rift Region (Western Branch of East African Rift). *Seismol. Res. Lett.* **88**, 49–60 (2017).

91. Geirsson, H. et al. Volcano-tectonic deformation in the Kivu Region, Central Africa: Results from six years of continuous GNSS observations of the Kivu Geodetic Network (KivuGNet). *J. Afr. Earth Sci.* **134**, 809–823 (2017).

92. Watson, L. M. et al. Volcano infrasound: progress and future directions. *Bull. Volcanol.* **84**, 44 (2022).

93. Smink, M. M. E., Assink, J. D., Bosveld, F. C., Smets, P. S. M. & Evers, L. G. A three-dimensional array for the study of infrasound propagation through the atmospheric boundary layer. *J. Geophys. Res.* **124**, 9299–9313 (2019).

94. Watson, L. M. et al. Infrasound radiation from impulsive volcanic eruptions: nonlinear aeroacoustic 2D simulations. *J. Geophys. Res. Solid Earth* **126**, 1–28 (2021).

95. Yamakawa, K. et al. Azimuth estimations from a small aperture infrasonic array: test observations at Stromboli Volcano, Italy. *Geophys. Res. Lett.* **45**, 8931–8938 (2018).

96. Johnson, J. B. & Ronan, T. J. Infrasound from volcanic rockfalls. *J. Geophys. Res. Solid Earth* **120**, 8223–8239 (2015).

97. Balagizi, C. M., Kasereka, M. M., Cuoco, E. & Liotta, M. Influence of moisture source dynamics and weather patterns on stable isotopes ratios of precipitation in Central-Eastern Africa. *Sci. Total Environ.* **628–629**, 1058–1078 (2018).

98. Perttu, A. et al. Remote characterization of the 12 January 2020 eruption of Taal Volcano, Philippines, using seismo-acoustic, volcanic lightning, and satellite observations. *Bull. Seismol. Soc. Am.* **113**, 1471–1492 (2023).

99. Waxler, R., Hetzer, C. H., Assink, J. D. & Blom, P. A two-dimensional effective sound speed parabolic equation model for infrasound propagation with ground topography. *J. Acoust. Soc. Am.* **152**, 3659–3669 (2022).

100. Blom, P. Modeling infrasonic propagation through a spherical atmospheric layer—Analysis of the stratospheric pair. *J. Acoust. Soc. Am.* **145**, 2198–2208 (2019).

101. Giordano, D. et al. Thermo-rheological magma control on the impact of highly fluid lava flows at Mt. Nyiragongo. *Geophys. Res. Lett.* **34**, L06301 (2007).

102. Mastin, L. G. A numerical program for steady-state flow of Hawaiian magma-gas mixtures through vertical eruption conduits. *U.S. Geol. Surv. Open-File Report*, 95–756 <https://doi.org/10.3133/ofr95756> (1995).

103. Wilson, L. & Head, J. W. Ascent and eruption of basaltic magma on the Earth and moon. *J. Geophys. Res.* **86**, 2971–3001 (1981).

104. d’Oreye, N., Derauw, D., Samsonov, S., Jaspard, M. & Smittarello, D. MaSTer: a full automatic multi-satellite InSAR mass processing tool for rapid incremental 2D ground deformation time series. in *Proc. 2021 IEEE International Geoscience and Remote Sensing Symposium (IGARSS)* 1899–1902 (IEEE, 2021).

Acknowledgements

We acknowledge former support from the Belgian Science Policy Office (Belspo) and the Fonds National de la Recherche (FNR) of Luxembourg through the RESIST project (Contract SR/00/305) for the development of the seismic/infrasound KivuSNet network used as telemetered, real-time monitoring network between 2015 and 2022 by the Goma Volcano Observatory (GVO). The GVO hosted GOM station and contributed to the maintenance of the network. Special thanks to Dr. Josué Subira, Dr. Adalbert Syavulisembo and Dr. Katcho Karume for their collaboration, as well as the Congolese Institute for Nature Preservation (ICCN) for hosting stations (KBTI, NYI) in the Virunga National Park. The authors would also like to thank Leighton Watson, Sylvie Vergniolle and one anonymous reviewer for their comments that helped to improve the former manuscript.

Author contributions

N.d.O., A.O., and J.B. conceived the network infrastructure, deployed the instruments in the field, and participated in the maintenance. J.B. performed the processing of local (DRC) seismic and infrasound data. J.B. performed the acoustic resonance modeling. J.A. performed the processing and modeling of distant (Kenya) infrasound data. N.d.O. provided the processed SAR amplitude images. J.B. and A.O. analyzed the results. J.B., A.O., J.A., N.d.O., and L.E. took part in the data interpretation. J.B. wrote the manuscript draft and made the figures. J.B., A.O., J.A., N.d.O., and L.E. contributed to the final version of the manuscript.

Competing interests

The authors declare no competing interests.

Additional information

Supplementary information The online version contains supplementary material available at <https://doi.org/10.1038/s43247-025-02937-3>.

Correspondence and requests for materials should be addressed to Julien Barrière.

Peer review information *Communications Earth & Environment* thanks Leighton Watson, Sylvie Vergniolle and the other anonymous reviewer(s) for their contribution to the peer review of this work. Primary handling editors: Sébastien Valade, Carolina Ortiz Guerrero, and Martina Grecequet. A peer review file is available.

Reprints and permissions information is available at <http://www.nature.com/reprints>

Publisher's note Springer Nature remains neutral with regard to jurisdictional claims in published maps and institutional affiliations.

Open Access This article is licensed under a Creative Commons Attribution-NonCommercial-NoDerivatives 4.0 International License, which permits any non-commercial use, sharing, distribution and reproduction in any medium or format, as long as you give appropriate credit to the original author(s) and the source, provide a link to the Creative Commons licence, and indicate if you modified the licensed material. You do not have permission under this licence to share adapted material derived from this article or parts of it. The images or other third party material in this article are included in the article's Creative Commons licence, unless indicated otherwise in a credit line to the material. If material is not included in the article's Creative Commons licence and your intended use is not permitted by statutory regulation or exceeds the permitted use, you will need to obtain permission directly from the copyright holder. To view a copy of this licence, visit <http://creativecommons.org/licenses/by-nc-nd/4.0/>.

© The Author(s) 2025